TECHNICAL UNIVERSITY OF LIBEREC
Faculty of Mechanical Engineering

# Experimental and numerical investigation of the metal sheets for automotive

## Master thesis

*Study programme:* N2301 – Mechanical Engineering
*Study branch:* 2302T010 – Machines and Equipment Design

*Author:* **Shehab Ashraf Salem**
*Supervisor:* prof. Ing. Karel Fraňa, Ph.D.

Liberec 2018

**Technical University of Liberec**
**Faculty of Mechanical Engineering**
Academic year: **2017/2018**

# DIPLOMA THESIS ASSIGNMENT

(PROJECT, ART WORK, ART PERFORMANCE)

| | |
|---|---|
| First name and surname: | **Shehab Ashraf Salem** |
| Study program: | **N2301 Mechanical Engineering** |
| Identification number: | **S16000459** |
| Specialization: | **Machines and Equipment Design** |
| Topic name: | **Experimental and numerical investigation of the metal sheets for automotive** |
| Assigning department: | **Department of Power Engineering Equipment** |

## Rules for elaboration:

The structured metal sheets are commonly used in many applications and recently can be found in many parts of the car starting from the car bodywork up to the engine space. Just in this last mentioned application the metal sheets protect the car inside environment against noise and heat load. The objective of the work will be a study of the structures on the noise and heat damping in relation to the car interior. The verification of the numerical and experimental approaches will be studied as well. This work will be carry out in a collaboration with a German university. The condition of the work is a short-term stay at the university in Germany. The assumed result: a selection of the appropriate structure in respect of the main protection function of the metal sheets.

Scope of graphic works:

Scope of work report
(scope of dissertation): **up to 50 pages**

Form of dissertation elaboration: **printed**

Language of dissertation elaboration: **English**

List of specialized literature:

[1] **R.L.Webb, N.Kim,** *Principles of Enhanced Heat transfer.* **Taylor-Francis, 2005, ISBN 1-59169-014-5.**

Tutor for dissertation: **prof. Ing. Karel Fraňa, Ph.D.**
Department of Power Engineering Equipment

Date of dissertation assignment: **1 February 2018**

Date of dissertation submission: **1 August 2019**

prof. Dr. Ing. Petr Lenfeld
Dean

L.S.

doc. Ing. Václav Dvořák, Ph.D.
Head of Department

Liberec, dated: 28 February 2018

**Declaration**

I hereby certify that I have been informed that Act 121/2000, the Copyright Act of the Czech Republic, namely Section 60, Schoolwork, applies to my master thesis in full scope. I acknowledge that the Technical University of Liberec (TUL) does not infringe my copyrights by using my master thesis for TUL's internal purposes. I am aware of my obligation to inform TUL on having used or licensed to use my master thesis in which event TUL may require compensation of costs incurred in creating the work at up to their actual amount. I have written my master thesis myself using literature listed therein and consulting it with my supervisor and my tutor. I hereby also declare that the hard copy of my master thesis is identical with its electronic form as saved at the IS STAG portal.

Date: 21/5/2018

Signature: Shehab Sabeen

*“We humans are a minority of giants stumbling around in a world of little things.”*

*Sue Hubbell*

# Acknowledgement

I would like to express my gratitude for my supervisor prof. Karel Frana for his guidance during this work. Also, I would like to thank Mr. Petr Kulhavý for providing me with the 3D scanned data of the sheets under investigation to perform the simulation. I would also like to show my gratitude to both of Mr. Jan Hůjer and Tomaš Kořinek for their continuous support and guidance regarding the lab work and numerical simulation. Finally, I would like to thank my family and friends with whom I am most fortunate.

# Abstract

This report investigates the aero-acoustic noise generated by sheet metals of three different structures. The investigation is done both experimentally and numerically in order to find the sheet of best acoustic performance. Each sheet was tested experimentally in a wind tunnel in the velocity range of 9 to 20 m/s where the produced sound was recorded by a microphone. The experiment aimed at finding which sheet produces louder noise. Moreover, the velocity fluctuation after the sheets trailing edge was captured by a Hot Wire Anemometer to find the dominant frequency of vortices and calculate turbulence intensity. Finally, the case of highest velocity was numerically simulated using Ansys fluent where the simulation was validated by the experimental results. The numerical analysis used LES turbulence model with Kinetic Energy Transport sub-grid model. Ffowcs-Williams & Hawkings model was used to predict the acoustic sources. Agreements were found between the trend of acoustic noise produced from experiment and numerical simulation over some ranges of frequency.

**Keywords :** *CFD, Ansys Fluent, Aero-Acoustic, Ffowcs-Williams & Hawkings*

# Table of Contents

# List of Figures:

## *List of Used Symbols:*

| *Symbol* | *Physical Quantity* | *Unit* |
|---|---|---|
| $S_{ij}$ | *Rate of Strain Tensor* | $s^{-1}$ |
| $\dot{q}$ | *Rate of change of Mass flow rate due to acoustic wave* | $[Kg/s^2]$ |
| $\mu_t$ | *Sub-grid Turbulent Viscosity* | *[Pa.s]* |
| $\tau_{ij}$ | *Sub-Grid Stress Tensor* | *[Pa]* |
| *C* | *Sound Velocity in air* | *[m/s]* |
| *f* | *Frequency* | *Hz* |
| *k* | *Turbulence Kinetic Energy* | *[J/Kg]* |
| *L* | *Characteristic Length* | *[m]* |
| *Ma* | *Mach Number* | *[-]* |
| *N* | *Overall mesh Length* | *[m]* |
| P | *Pressure* | *[Pa]* |
| *Re* | *Reynold's Number* | *[-]* |
| *S* | *Surface Area of Vibrating Body* | $[m^2]$ |
| *SPL* | *Sound Pressure Level* | *dB* |
| *St* | *Strouhal Number* | *[-]* |
| *t* | *Time* | *[Seconds]* |
| *T* | *Lighthill Stress Tensor* | *[Pa]* |
| *U* | *Velocity* | *[m/s]* |
| *V* | *Vibration Velocity* | *[m/s]* |
| *W* | *Sound Power* | *[Watt}* |
| $\sigma_{rad}$ | Sound radiation efficiency | *[-]* |
| $\rho$ | *Density* | $[Kg/m^3]$ |
| $\omega$ | *Turbulence specific Dissipation Rate* | $[s^{-1}]$ |
| $\epsilon$ | *Turbulence Dissipation Rate* | *[J/(Kg.s)]* |

## *List of used Abbreviations:*

| *Abbreviation* | *Meaning* |
|---|---|
| *DES* | *Detached Eddy Simulation* |
| *DNS* | *Direct Numerical Simulation* |
| *FFT* | *Fast Fourrier Transform* |
| *LES* | *Large Eddy Simulation* |
| *RANS* | *Reynold Averaged Navier Stoke's Equation* |
| *SGS* | *Sub-Grid Scale* |
| *SST* | *Shear Stress Transport* |
| *TBL* | *Turbulent Boundary Layer* |

# 1. Introduction:

Nowadays, Ergonomics is gaining more and more consideration in the field of automotive design. This consideration aims at giving better experience for the car passenger from the comfort point of view. Among the criteria used to assess comfort of a certain vehicle is the level of noise perceived by its passengers. A machine as complex as a car would involve tremendous number of noise sources which would together play a complex melody. These sources would include for example the tires /road interface. It would include also the aerodynamic noise sources inhibited in the car body with all its fine details (e.g side mirrors, sun roof). This noise depends on vehicle's external geometry which may cause flow separation that results in strong pressure fluctuations, as will be discussed later in more details. Finally, there is the drive train noise source which is already a collection of different sources including the engine intake system, pistons, exhaust manifold, cooling system and the gear box. These sources would collectively produce different kinds of noise, tonal or broadband, using various mechanisms of sound production to eventually give the passenger the normal car sound that they are used to. [1]

However, with recent developments in the performance of drivetrain in general, the noise generated by these sources has been reduced or at least damped inside the car interior. This leaves the aerodynamic generated noise to be the significant source especially at the speeds of 100 Km/h. Figure 1 shows an example of the sound pressure levels produced by different sources over different frequencies where aerodynamic noise comes generally in the second place after the tires/road noise. [2]

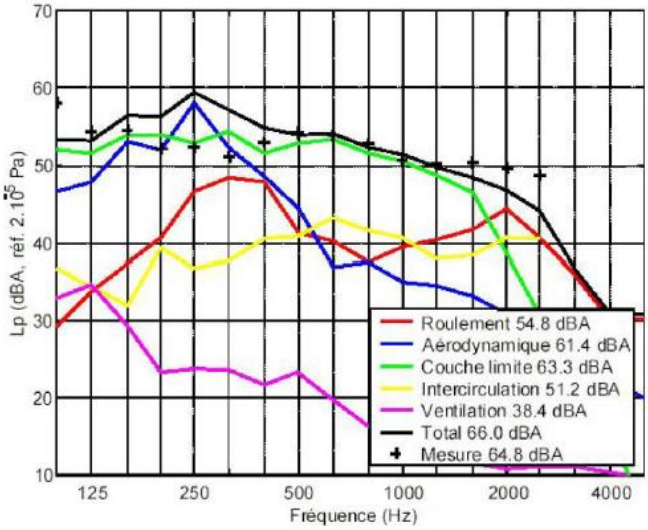


*Figure 1 Different contributions to automotive noise: "Roulement": road noise, "A´erodynamique": aerodynamic noise, "Couche limite": boundary layer noise, "Interrecirculation": recirculating flow, "Ventilation": air cooling noise. From* [2]

On reviewing the previous literature devoted for the field of Aero-acoustic of Auto-motives, it was found that a lot of work has been done on different parts of the car. Among the parts that have been addressed most is the car side mirrors. An example of such study is presented below. Also, another study aiming at the performance of car bonnet is mentioned.

## 1.1. Analysis of a Car Side Mirror:

Wang et Al [3] studied flow of velocity 38.9 m/s over a generic model of a side mirror by applying CFD simulation using Ansys fluent. In the analysis, they used simple model of a generic side mirror resembling that was used in the practical experiments done by Siegert et Al and Hold et Al so that their experimental results can be used for the sake of validation of simulation. The analysis was performed once with LES model and another with DES model in order to compare the acoustic results of the two models.

The model, as shown in Figure 2, is composed of a squared cylinder of dimension 0.2 m topped by a quarter of a sphere of the same dimension. The mirror is placed over a flat plate of 1.6 by 2.4 m dimensions. They developed mesh using the commercial software ICEM-HEXA. The mesh was built by an unstructured hexahedral elements with edge length kept at 0.003 meters on the mirror and on the base plate in the vicinity of the mirror. Fine mesh was created in the wake of the mirror till a distance of 1 meter from the mirror's rear face. The mesh was progressively coarsened from the vicinity of the mirror to the domain boundary where the mesh edge length was kept at 0.1 meter. Figure 4 and Figure 5 show the constructed mesh.

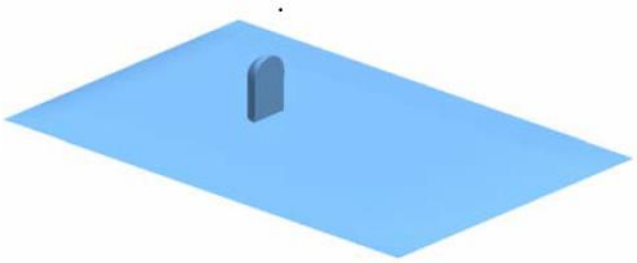

*Figure 2 Generic Side mirror and its base plate in the model of Wang et Al.*

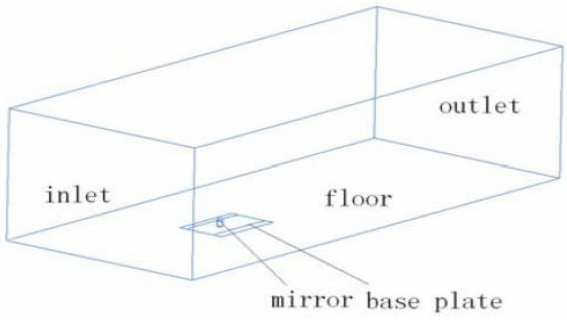


*Figure 3 The Computation domain in the model of Wang et Al.*

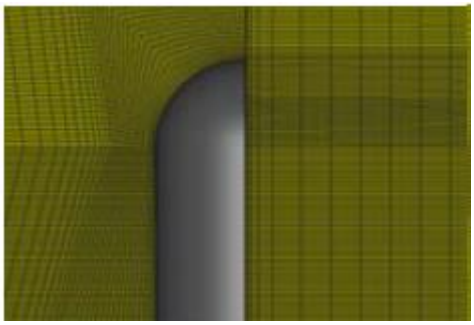

*Figure 4 Front View of mesh used by Wang et Al.*

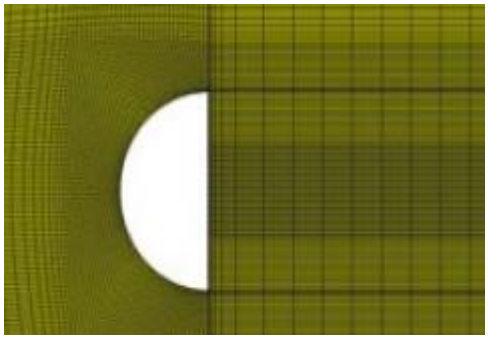

*Figure 5 Top View of mesh used by Wang et Al.*

Finally, as was mentioned before, the problem was solved twice. The first time was using LES model with Lily Smagorisnky model for sub-grid viscosity while the second time was using DES model based on realizable k - $\epsilon$ model. Table 1 summarizes the used boundary conditions while Table 2 summarizes the used solver settings. The simulation for the both cases was initialized using a steady-state analysis using RNG k - $\epsilon$ model and 2$^{nd}$ order discretization schemes. Then, transient analysis was performed with time step of 0.003 seconds till the solution reached dynamic stability. Then, further real analysis with time step of 0.0001 seconds was performed to extract the acoustic results. Pressure probes were set up at locations that agrees with those used in the experiment as shown in Figure 6 and Figure 7.

*Table 1 Boundary Conditioin in Model of Wang et Al*

| Boundary | Boundary Condition | Value |
|---|---|---|
| Inlet | Constant Velocity | 38.9m/s |
| Outlet | Constant Pressure | 0 Pa (gauge) |
| Floor | Symmetry | - |
| Other wall | Free slip wall | - |
| Mirror | No slip wall | - |
| Plate | No slip wall | |

*Table 2 Solver Settings used by Wang et Al.*

| Function | Setting |
|---|---|
| solver | Segregated implicit Double precision |
| Time-stepping | 2nd order implicit |
| Pressure discretization | 2nd order |

| | |
|---|---|
| Momentum discretization | 2nd order upwind |
| Pressure-velocity coupling | SIMPLE |
| Fluid | Air |

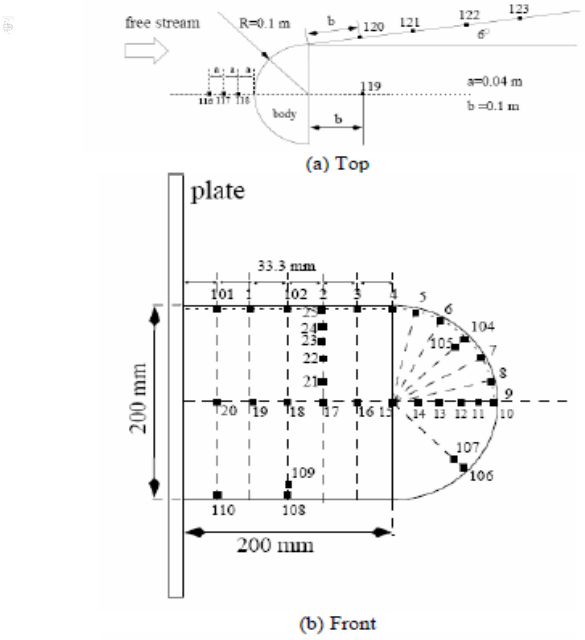


*Figure 6 Locations of Pressure Probes (Front and Top Views*

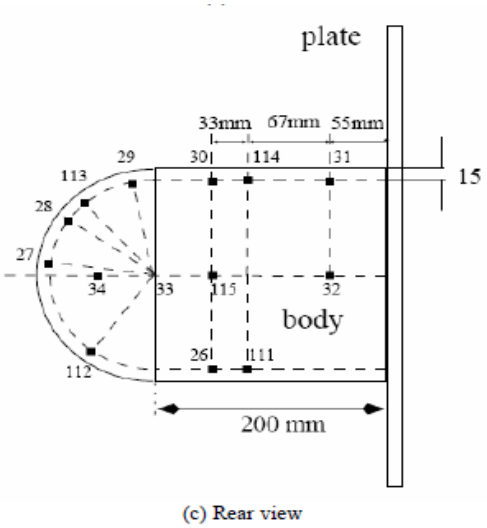


*Figure 7 Locations of Probes (Side View)*

**Results:**

- The two models gave good agreement with the practical results as shown in Figure 8.
- The mirror cause complex wake with eddies on a wide scale using the two turbulence models as shown in Figure 9. From that figure, it can be noticed that the shear layers over the cylindrical part of the mirror are the dominating cause to the sound generation. Also, by comparing the results from the LES and DES models, it can be noticed that the club-shaped structures are less pronounced in the DES simulation the high intensity region is smaller than the LES results.
- Separation region extends for a distance roughly double the mirror height.

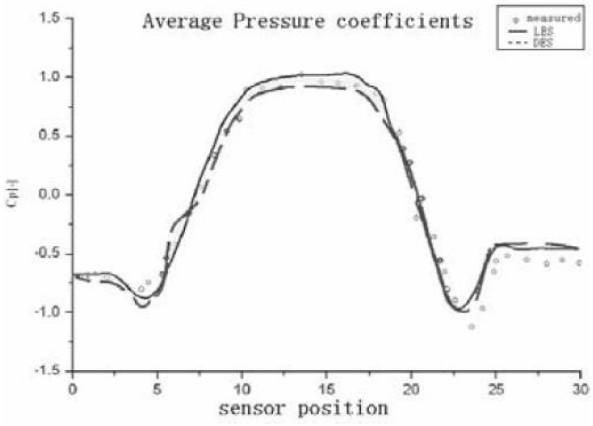


*Figure 8 Comparison of Numerical and Experimental Results*

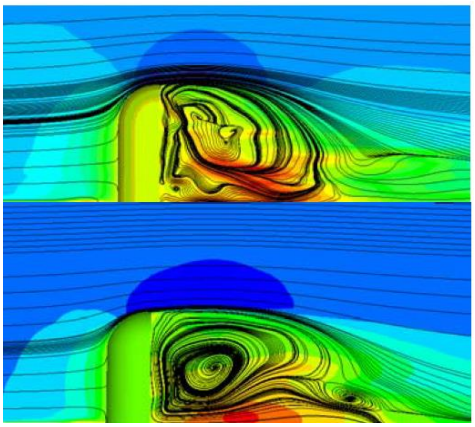

*Figure 9 Instantaneous velocity contours and streamline along the symmetry returned by LES (up) and DES (down)*

- The wall pressure fluctuations obtained at different locations, (114, 116, 121 and 123), from both of the two simulations as well as from the experiment results were calculated and compared. From the comparison it was possible to notice that:

    - The DES model prediction is quite accurate below 100 Hz and under-predicts the sources of frequency over 100 Hz. On the other hand, LES model predicts the levels fairly accurate all the way.
    - A general trend for the wall pressure results is that the levels are under-predicted by the DES model but over-predicted with the LES approach. An over-prediction would intuitively be expected due to the incompressible assumption, but at the same time LES will expend much more computer source than DES, so the selection of LES or DES must be caution in practical engineering applications. [3]

## 1.2. Analysis of Airflow around a Kink shaped Auto-Mobile Bonnet:

Yokoyama et Al. [4] investigated the acoustic radiation produced by the airflow flow around a curvilinear body with a kink shape. To clarify the mechanism and condition for the radiation of these noise, wind tunnel experiments were performed over the model. Several configurations were experimented with different flow velocities as well different angle of orientation of the kink $\gamma$ with respect to the flow direction. The produced noise was recorded by means of a 0.5 inch microphone placed 800 mm

perpendicular to the kink. Moreover, the flow speed $U_{ref}$ was measured by means of constant temperature hot wire anemometry at various locations that lie $x_d$ $and$ $y_d$ $away$ from the origin placed at the kink. Figure 10 shows a schematic of their experimental set up.

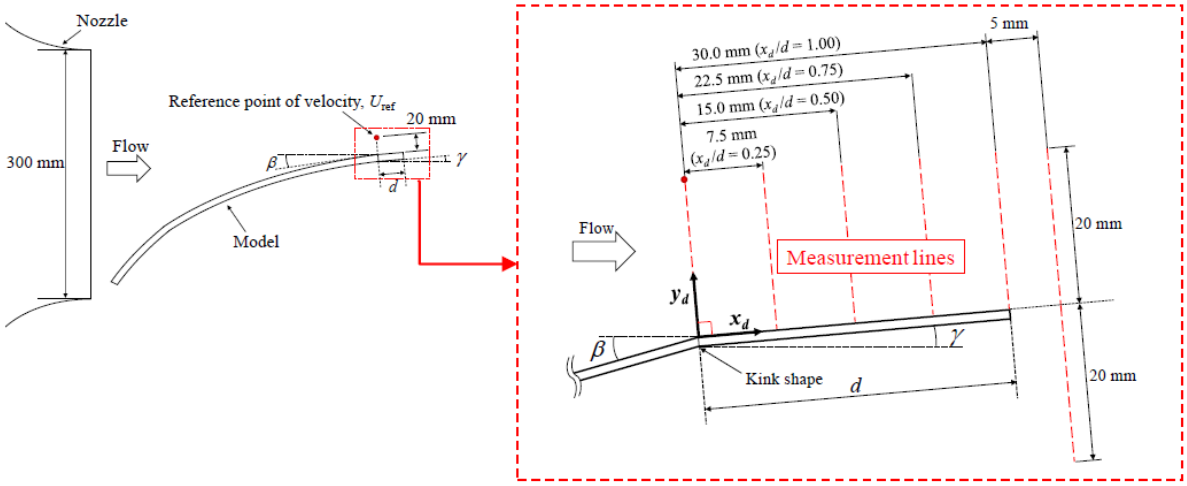


*Figure 10 Experimental Set-up of Yokoyama et Al.*

**Results:**

- As shown in Figure 11, there are certain configurations that produce tonal noise of high peaks, $\gamma = 5^o$ $and$ $\gamma = 10^o$.
- Figure 12 shows the relation between the strength of the produced tonal noise and the airflow speed, normalized to the sound speed in form of Mach Number, at different orientation angles. It can be noticed that for the case of $\gamma = 10^0$, the SPL tends to grow with increasing speed to reach maximum SPL of 77 dB at airspeed of 0.104 Ma, $U_{ref} = 36\ m/s$.
- On the other hand, the strength of the produced tone tends to drop with increasing speed in the case of $\gamma = 5^o$. It achieves maximum SPL of 63 dB at flow speed of 0.076 Ma, 26 m/s. The authors account this behavior to the fact that the flow separation in the downstream of the kink is larger and the flow around the kink shape becomes turbulent as the velocity increases.
- Figure 13 and Figure 14 show the effect of airspeed on the Strouhal number of the peak noise. They found that The dominant peak frequency jumps from St = 2.5 to St = 3.0 at $M_{ref}$ $of$ 0.082 ($U_{ref} = 28\ m/s$). This ladder-type behavior was also observed in flows around an airfoil in past

research. This would indicates that the acoustic-fluid interactions occur in the present configurations like in flows around an airfoil. [4]

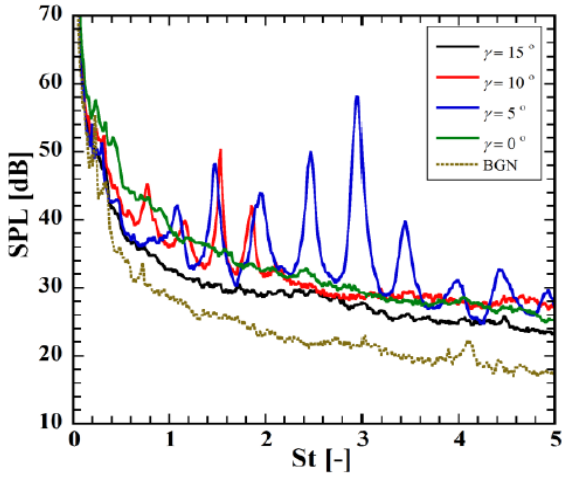


*Figure 11 Effect of orientation angle on the produced tonal noise*

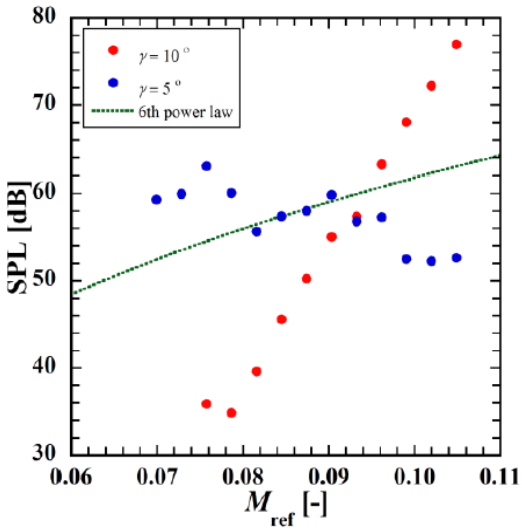


*Figure 12 Effect of Airspeed on the produced tonal noise.*

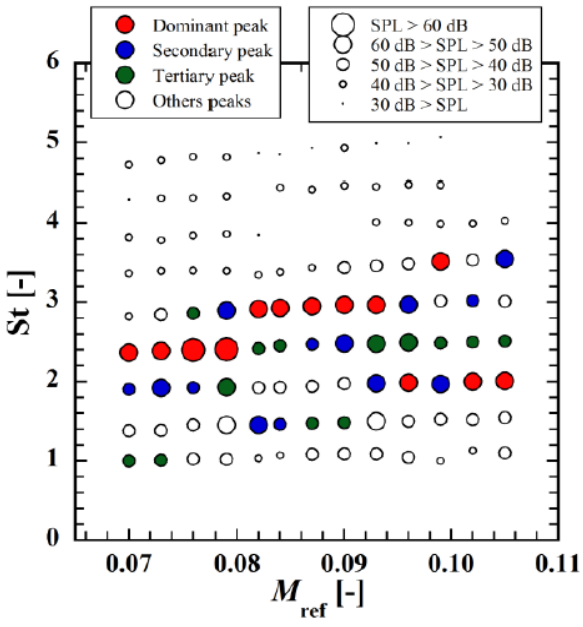


*Figure 13 Effect of airspeed on the Strouhal number of peak noise for $\gamma = 5^o$*

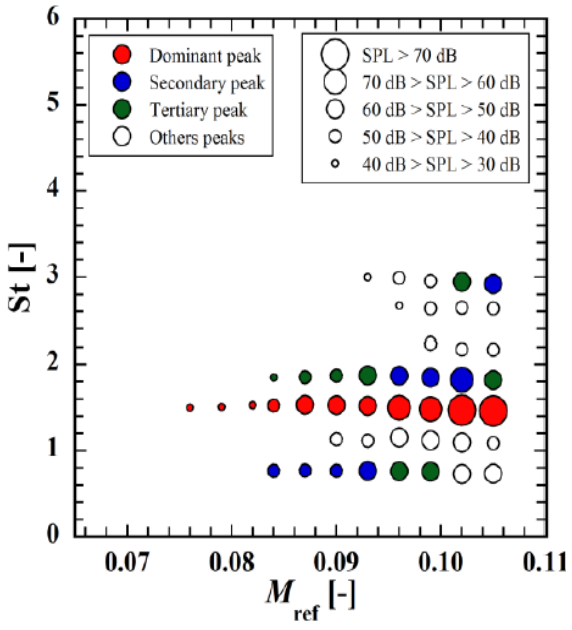


*Figure 14 Effect of airspeed on the Strouhal number of peak noise for $\gamma = 10^o$ according to*

## 1.3. The Aim of the Thesis:

Finally, the aim of this project is to study the acoustic performance of structured sheet metals which are used in car industry. To serve this goal, sheets of three different structures, named KMT, PWO and WAB, are investigated. The investigation is done by means of wind tunnel experiments as well as numerical simulation using Ansys Fluent software. The report starts by the introduction which presents the motivation to do such a project as well as examples of similar previous research. Then, chapter (2) provides background about the theory behind sound Acoustics in general as well as Aero-Acoustics. It also discusses briefly the LES turbulence model which was recruited in this analysis. Then, chapter (3) discusses the experiments performed on the sheets. Eventually, chapter (4) discusses the numerical simulations of the problem. Finally, chapter (5) provides a summary of the results reached by this work.

# 2. Theoretical Background:

## 2.1. Noise Specification:

What is sound? Sound, in essence, occurs as a result of pressure fluctuation. This pressure fluctuation would cause the transporting medium to vibrate in a series of successive compressions and rarefactions. These compression and rarefactions cause a pressure wave to flow along the medium till it strikes a human ear drum. Eventually, this pressure fluctuation is perceived by the ear.

As a wave, noise is defined in terms of amplitude and frequency. The amplitude refers to the amplitude of the pressure. However, this absolute pressure value is not informative on how much strong this noise is. Thus, it is usually referred to in relative to a reference value of pressure which would cause the threshold of sound perception in human ears. This ratio normally has a very wide range. Hence, usually the log of this ratio is considered and multiplied by factor of 20 and defined as Sound Pressure Level, or SPL, such that:

(1)

$$SPL = 20\log(\frac{P1}{P2})$$

Where $P_1$ and $P_2$ are the pressure values of the wave and ear threshold respectively. Up to this point, the sound produced by the source has been considered. Now, it is time to take into consideration how this sound is perceived in order to be able to select the suitable mode for sound measurement. Human ear can detect frequencies ranging from 20 up to 20,000 Hz. However, it does not perceive all sounds of all frequencies with the same sensitivity. Human ear is most sensitive to sounds of frequencies ranging from 0.5 to 6 KHz. Sounds of frequencies outside this range would be perceived with less sensitivity till this sensitivity vanishes when the sound is of frequency outside the hearing range. (20 to 20 KHz). Thus, some filtration models have been applied to simulate how the ear perceives sound. [5]

## 2.2. dB (Z), dB(A) and dB(C):

Assuming there is a sound source that emits waves of the same SPL at any frequency, this source would be modeled by weighting Z and measured in dB (Z). This weighting model does not involve any correction on the produced sound. However, the human ear would perceive the sound waves of this source with a different SPL depending on its frequency. To express the SPL perceived by the ear, weighting (A) filter was

developed in a way such that it gives greatest weight to sounds of mid-range frequency and less weight to sound of frequencies lying in the two extremes of the hearing range. Then, the filter totally nullifies sounds of frequency outside of the hearing range.

However, it was found that human ear's sensitivity is not only function of sound frequency, but also function of the sound SPL. At high SPL, ear sensitivity to low frequencies increases. Thus, weighting C filter was developed in a way such that it gives higher weight to low frequencies than A weighting filter. Figure 15 clarifies the three filters. It is worth mentioning that the three filters are defined to be normalized at frequency of 1 KHz. [6]

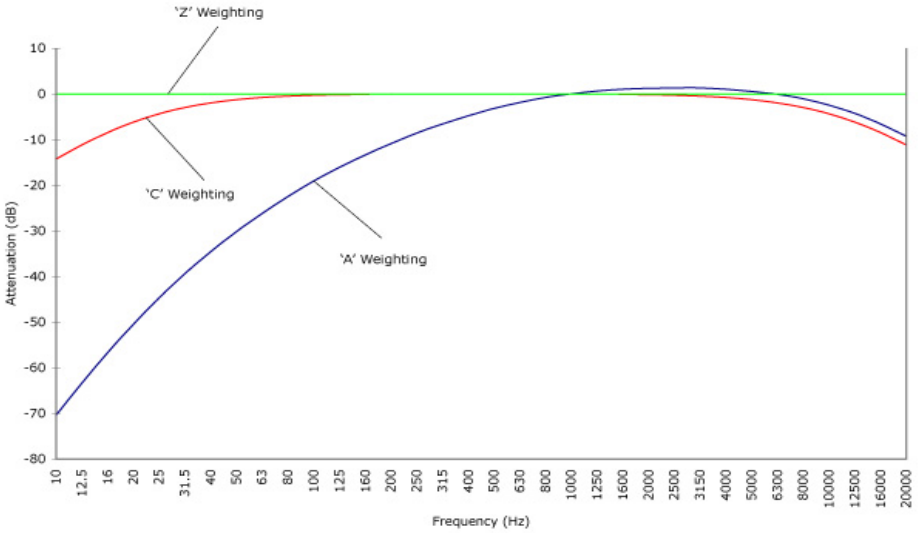


*Figure 15 Relation between Different Weighting filters*

Usually, filter based on weighting A is used when the interest is in how much the ear is ok, how much it can perceive sounds that it should be able to perceive. On the other hand, weighting C filter is used to study the peak sound level or to monitor the very low and high frequencies that workers are subjected to in a factory for example. Finally, weighting Z, since it is not concerned with sound receiver at all, may be used for the sake of comparison of different sound sources. [7] In the experimental work that is going to

be discussed later, the goal is to study the sound sources inherited in the flow over sheet metals. Therefore, the best filter to use would be the Z filter.

## 2.3. Noise Types:

As was discussed before, Sound is nothing but a propagating pressure wave. However, this pressure wave could be formed due to different reasons. For example, it can be a result of vibration of a solid body which would result in what is known as **Mechanically Generated Sound.** On the other hand, it could be formed as result of fluid flow to result in what is known as **Aero-dynamically Generated Sound.** In the next section, the two types of sound shall be elaborated with giving more space to the later as it is of more concern to the application of this project.

### 2.3.1. Mechanically Generated Noise:

Mechanically generated noise is generated when a solid body vibrates causing the surrounding medium to vibrate in return. The vibrations occur in a series of successive compressions and rarefactions with the system natural frequency. A solid vibrating surface would produce sound of power (W) related to the body surface area (S) as well as its vibration velocity such that:

$$W = \rho\, C\, S\, V^2\, \sigma_{rad} \tag{2}$$

Where $\rho$ is the medium density, C is the sound velocity in air, V is the vibration velocity and $\sigma_{rad}$ is the radiation efficiency that expresses how much of the vibration energy is transported to the surround medium and not stuck in the vibrator. Usually, to generate the mechanical noise, it is possible to reduce the vibrating area by dividing the large area into smaller areas by means of a flexible joint. The other option would be by reducing the vibration velocity. [8]

### 2.3.2. Aero-dynamically Generated Noise:

To produce sound, it is needed to have pressure fluctuation. For mechanically generated noise, the fluctuations were obtained by mechanical vibration of solids. However in the case of Aero-dynamic sound, we find that the required pressure fluctuations can emerge in a steady jet although that the jet was, initially, totally free of any fluctuations by implementing some instabilities. Moreover, the generated sound can be amplified in a feedback mechanism if the flow was intercepted in a certain conditions by a body or a cavity. It is interesting to mention that the flow of air through a cavity is the principal on which

wind instruments as organ are based. [9] In the next section, the two processes are discussed in more details.

If an air jet flowing inside a channel is discharged through a nozzle to the atmosphere, mixing regions are developed between the jet region and the atmosphere. In these regions, an unstable free vortex layer is formed generating disturbances along the stream as shown in Figure 16. Moreover, if these disturbances occur with the adequate frequency, it would result in the vortices reacting together causing disturbance furtherly getting amplified and the turbulence to grow along the flow causing the generation of aero-dynamic sound. [9]

It is worth mentioning that each jet diameter would have its characteristic disturbance frequency range that would result in growth of disturbances. Moreover, this frequency range depends on the jet Reynold's number (Re). At a high Reynolds number, there is a wide range of exciting frequency and this range would result in high growth of disturbance. However, at a lower Re, this range is narrower and of less amplification property. Figure 17 clarifies the relation between exciting frequency and the disturbance amplification. [9]

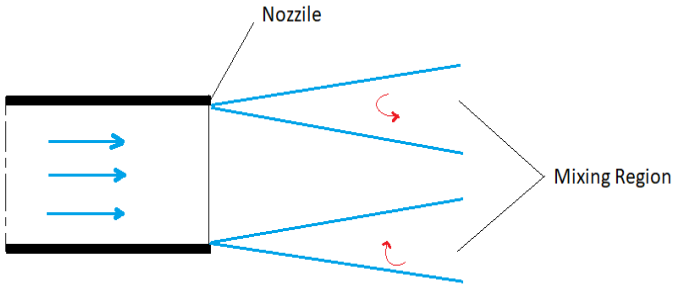


*Figure 16 Discharge through Nozzle at Atmosphere*

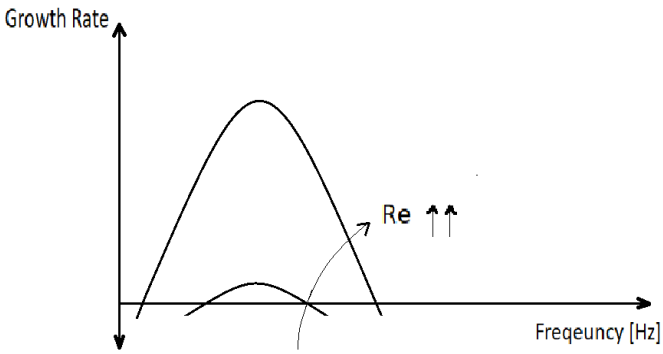


*Figure 17 Relation between Excitation frequency and Reynolds Number.*

However, for a flow of low Reynold's number, it is still possible to obtain more growth by implementing a feedback mechanism. In this case, an external factor is introduced such that when the instability interacts with this factor, it starts reacting in the reverse way changing the flow parameters causing more instability in the flow. This factor can be in the sound generated due to the forward direction instabilities or a body

immersed in the flow, a cylinder or a sheet metal. This body would cause further vortex shedding known as Karman vortices. [9]

In general, oscillating fluid structures can be described by a dimensionless number defined as Strouhal Number (St). Strouhal number is the ratio between the inertial force due to the change in in velocity due to the generated instability and the inertial force due to the fluid flow in the downstream direction. It is defined as:

$$St = \frac{f.l}{v} \tag{3}$$

Where *f* is the frequency of vortex shedding in Hertz, *l* is the characteristic length and *v* is the free stream velocity. Kovaszny obtained a critical value of *Re* of 40 at which vortex shedding would start to appear. Then for *Re* from 40 to 150, stable Karman Vortices Street would form. Then for *Re* from 150 to 300, the flow enters a transition stage between stability and turbulence where the relation between Strouhal number and *Re* is complex. Then for *Re* above 300, the flow becomes turbulent [10].

### *Aero-dynamic Noise Sources:*

After discussing how the sound is created, the next question would be how much the created sound is. To answer that question, it is important to specify that the considered sound energy is the energy that is radiated at the sound speed in ambient air. This energy would vary inversely with the radius. However, this energy does not represent all of the radiated energy since some of the radiated sound energy is radiated with speed of the flow speed not the sound speed. This portion of energy is the portion that results from the universal pressure difference in the flow and not from the turbulence. This sound energy can be heard as Pseudo-noise and can be found only in the near vicinity of the source. [9]

Lighthill studied the sound generation due to air flow. He identified three types of sound sources: simple (monopole), di-pole and quad-pole. Mono-poles are generally associated with mass fluctuation. Di-poles are associated with force fluctuation while quad-poles are associated with moment fluctuation. [11] In the next section each source is discussed in details.

**Mono-Pole:**

A mono-pols is a simple source that radiates equal energy in all directions. It radiates energy due to fluctuation of mass flow rate. Thus, it is always found in cases of pulsating flow. The pressure drop at a radius ***r*** and time ***t*** can be related with the rate of change of the mass flow rate by:

$$\Delta P = \frac{\dot{q}.(t - \frac{r}{c})}{4\Pi r} \tag{4}$$

Where *c* is the sound speed in ambient air, $\Delta P$ is the pressure drop and $\dot{q}$ is the resultant rate of change of mass flow rate which also refers to the source strength. Intensity of radiated energy varies with $U^4$ at high velocities.

**Di-Pole:**

A di-pole source is formed when two mono-poles of equal strength and opposite phases are located next to each other with a distance of *l* in between as shown in Figure 18. As mentioned before, it is associated with cases of fluctuating force as a result of vortex shedding. Opposite to mono-poles, they don't radiate energy equally in all direction. In fact, in east and west directions, energy of the two sources nearly, but not totally, cancels out.

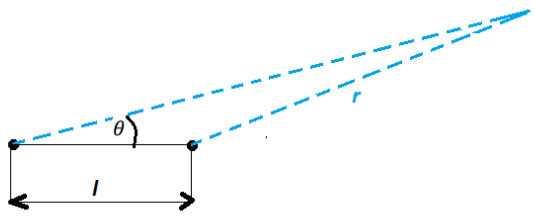


*Figure 18 A di-Pole Source*

For a dipole, it is important to define the near field and far field. Near field is the space around the di-pole with radius nearly equals to the wave length of the acoustic wave. Far field wave is the space at distance bigger than the wave wavelength. The pressure drop due to a di-pole is calculated as the sum of the pressure drop due each of the two mono-poles. Therefore, the total pressure drop at a radius ***r***, angle $\boldsymbol{\theta}$ and time ***t*** can be related with the rate of change of the mass flow rate by:

$$\Delta P = \frac{\dot{q}.\left(t - \frac{r}{c}\right) l.\cos(\theta)}{4\Pi r.r} + \frac{\ddot{q}.\left(t - \frac{r}{c}\right) l.\cos(\theta)}{4\Pi r.c} \tag{5}$$

Where again $c$ is the sound speed in ambient air, $\Delta P$ is the total pressure drop and $\dot{q}$ is the total rate of change of mass flow rate and $\ddot{q}$ is the second time derivative of mass flow rate. It refers to the source intensity. The first term in the equation dominates in the far field where the radiated energy varies inversely with r. It can be noticed that it is nothing but the pressure drop of a monopole scaled down by a ratio $l/r$ . Thus, we conclude that the dipole radiates less energy than a monopole of the same strength. On the other hand, the second term dominates in the near field and is scaled down from the mono-pole source by $\frac{2\,\Pi\,l}{\lambda}$. Intensity of radiated energy varies with $U^6$ at high velocities.

**Quadro-Pole:**

Similar to di-poles, quad-poles results when two di-poles are located next to each other. The two di-poles should be of the same strength and opposite in phase. They are associated with moment fluctuation which happens in turbulence due to jet streams. For the near field, since the quadrupole can be thought of as composed of 4 mono-poles, therefore its near field strength is scaled down from a mono-poles strength by$(\frac{2\,\Pi\,l}{\lambda})^2$. Therefore, quadrupoles are very inefficient radiators. Based on that, it can be concluded that the ratio between far and near pressure is varies with $U^2$ while the intensity of radiated energy varies with $U^8$ at high velocities.[12]

*Lighthill's Analogy:*

Lighthill studied an element volume in a very large fluctuating flow. The remainder of the fluid is assumed to be at rest. By comparing the equations governing the fluctuations inside the real fluid with a uniform acoustic medium at rest, a force field is acquired by calculating the difference between the fluctuating part and the stationary part. He derived the equation:

$$T_{ij} = \rho v_i v_j + p_{ij} - c_o^2 \rho \delta_{ij} \qquad (6)$$

Where T is the Lighthill strength tensor which describes the sources strength [11]. After demonstrating the theory behind aerodynamic sounds, the next section demonstrates the potential aerodynamic sounds sources inside a car.

## 2.4. Aero-Dynamic Sound Sources inside a Car:

A large part of the flow noise comes from turbulent fluctuations in airflow from the base of the windshield to the door post behind the driver which is the area where there are a lot of body angle changes and

openings. Aero-dynamic noise can be generated due to three reasons. Von Karman Vortices (due to air flow around the body components like rear view side mirrors), Separation of Boundary Layer and generation of cavities. The first two methods shall be discussed in some details since they are more relevant to the investigations covered in the report.

### 2.4.1. Wind Noise from Aerodynamic Components:

The noise generated due to airflow around an outside rea view mirrors, for example, is a major wind noise source at high speeds. It generates broadband noise of frequencies ranging from high frequencies, up to 5000 Hz, to a lower limit governed by the large alternate vortices shed from the top and bottom edges of the mirror. These coherent structures induce highly-energetic wake that resembles a von Karman vortex street, which impinges the side windows. In some car designs, fancy shapes, fins and strategically placed holes are added to allow air to flow around the mirror smoothly to minimize these effects.

Due to the high-Reynolds number, and the inherently 3-D geometry of the mirror, three-dimensional effects are very important. In order to evaluate the broadband noise directly radiated, or indirectly transmitted by the pressure loading, Large Eddy Simulation seems a good candidate. But the complexity of the configuration remains challenging for CFD industrial codes.

### 2.4.2. Turbulent Boundary layer noise:

The sound induced by the turbulent boundary layers developing on the car main body is of fundamental interest. The reason behind that is that these sound waves can cause pressure load on the car body that would excite vibrational modes of the car structure which would be harmful for the car body. Moreover, it may in return produce more sound.

The pressure fluctuations beneath a turbulent boundary layer (TBL) have been the subject of numerous experimental and theoretical studies. With the development of supercomputers, the numerical simulation constitutes a new efficient approach. The wall-pressure field generated by Direct Numerical Simulations (DNS) and Large-Eddy Simulation (LES) of channel flow has been massively investigated. Moreover, simplified semi-empirical models of wall-pressure fluctuations have been proposed. The most popular are Corcos' model and Chase's model [2].

### 2.4.3. Cavity Noise:

All the gaps present on the vehicle surface can constitute cavities excited by the turbulent boundary layers developing on the vehicle. These gaps include open windows, sunroof buffeting, and door gap cavities [2].

## 2.5. Turbulence Modeling:

The flow of any fluid around an object must achieve certain governing equations. The most important of these equations are the laws of conservation of mass, the continuity equation, and momentum, the Navier Stokes Equation ( N.S ). For a flow of Mach number less than 0.4, the behavior of this flow can be considered as incompressible. In such a case, the continuity and Navier Stokes equations can be written as in equations (7) and (8) respectively.

$$\frac{dv_i}{dx_i} = 0 \tag{7}$$

$$\rho \frac{dv_i}{dt} + \rho \frac{\partial v_i v_j}{dx_j} - \mu \frac{\partial^2 v_i}{\partial x_j \, \partial x_j} = -\frac{\partial p}{\partial x_i} \tag{8}$$

**Direct Numerical Simulation (DNS):**

For a fluid flowing at Reynold's number more than 5000, this fluid would be described as turbulent. In such a case, vortices known as "Eddies" start to develop and interact with each other. These vortices will have scales that range from small to large scales. The large eddies will provide the small eddies with energy until the whole turbulence energy is dissipated in the smallest Eddies. In case all the eddies were to be resolved accurately, which is a method known as Direct Numerical Simulation (DNS), it would be crucial to construct a mesh of element size smaller than the smallest eddy and yet, the whole mesh should have overall length (N) in any direction larger than the corresponding dimension of the largest eddy. In another words, the mesh should be large enough to include the whole of the largest eddy, and the mesh elements should be small enough to represent the smallest eddy. This is represented by equation (9) where N is the overall mesh length. However, these criteria would results in a very computationally expensive mesh and would limited to small Reynold number application only. [13]

$$N^3 \geq Re^{9/4} \tag{9}$$

**RANS Turbulence Models:**

To address cases of larger Reynold number, it was crucial to find an alternative other than resolving the whole scale of the developed eddies. Thus, RANS (Reynold Averaged Navier Stoke's) models were developed. The concept behind RANS models is to represent the flow parameters as a combination of a time-averaged component $\overline{v_\iota}$ and a fluctuating component $\grave{v_\iota}$ as follows:

$$v_i = \overline{v_\iota} + \grave{v_\iota}$$

In this case, we get equation (10) known as the Reynold's Averaged Navier Stoke's equation which is in terms of time averaged values and a new unknown stress tensor resulting from the fluctuating components known as Reynold stress tensor. There different models based on the RANS method that try to estimate the Reynold stress Tensor. The most common among these are the two equation models like k-ε and k-ω.

$$\rho \frac{d\bar{v}_i}{dt} + \rho \frac{\partial \bar{v}_i v_j}{\partial x_j} - \frac{\partial}{\partial x_j}(\mu \frac{\partial \bar{v}_i}{\partial x_j} + \rho \overline{\grave{v_\iota}\grave{v_J}}) = -\frac{\partial \bar{p}}{\partial x_i} \tag{10}$$

**Large Eddy Simulations (LES):**

In cases where there are very wide variety of eddy, it was found that solution based on time averaged values isn't reliable. Therefore, LES model was developed based on the theory of self-similarity. It states that the large eddies depend on the flow geometry and boundary conditions and must be calculated explicitly. However, the smaller eddies are independent on such parameters and possess some similarities among each other. Therefore, they can be modeled by a sub-grid scale models SGS. In fluent, the sub-grid turbulence tensor is calculated according to Boussinesq hypothesis such that:

$$\tau_{ij} = \frac{1}{3}\, \tau_{kk}\, \delta_{ij} - 2\mu_t \overline{S_{\iota J}} \tag{11}$$

Where $\mu_t$ is the sub-grid turbulent viscosity and $\overline{S_{\iota J}}$ is the rate-of-strain tensor for the resolved scale and defined by:

$$S_{ij} = \frac{1}{2}(\frac{\partial \overline{u_\iota}}{\partial \overline{x_J}} + \frac{\partial \overline{u_J}}{\partial \overline{x_\iota}}) \tag{12}$$

And by introducing the density weighted filter operator (FAVRE) where:

$$\phi = \frac{\overline{\rho\phi}}{\bar{\rho}} \tag{13}$$

The Favre Navier Stoke's equation can be written as:

$$\tau_{ij} = -\rho\, u_i\, u_j + \bar{\rho}\, u_i\, u_j \tag{14}$$

And representing the shear tensor as an isotropic and a deviatoric components:

$$\tau_{ij} = \frac{1}{3}\, \tau_{ll}\, \delta_{ij} + \tau_{ij} - \frac{1}{3}\, \tau_{ll}\, \delta_{ij} \tag{15}$$

Where the deviatoric component is modeled using the compressible form of Smagorinsky model such that:

$$\tau_{ij} - \frac{1}{3}\, \tau_{ll}\, \delta_{ij} = 2\mu_t(\delta_{ij} - \frac{1}{3}\delta_{ij}\delta ij) \tag{16}$$

FLUENT offers four models for computation of $\mu_t$ named as:

- Smagorinsky-Lilly model
- Dynamic Smagorinsky-Lilly model
- WALE model
- Dynamic kinetic energy sub grid-scale model.

Further information about these sub-grid models can be found in [14]. LES model is the most widely used model in academia. However, it is still not popular in industrial applications. One of the reasons is that the near wall region needs to be represented with an extremely fine mesh not only in the direction perpendicular to the wall but also parallel with the wall. This is because the turbulence length scale becomes very small near the wall relative to the boundary layer thickness. For this reason, LES is not recommended with flows with strong wall boundary effects. In other words, the flow should be irrelevant to the wall boundary layers. Moreover, LES needs excessive computational power due to the statistical stability requirement. Generally, the LES solver requires long computational times to reach a statistically stable state. Therefore, a substantially long preparation time is needed for a successful run of LES.

# 3. Experimental Test:

As discussed before, the goal of this work is to study acoustic radiation due to the flow across sheet metals of different structure configurations as shown in Figure 19, Figure 20 and Figure 21 . To serve this goal, wind tunnel experiment has been carried out where each of the sheets was placed inside a wind tunnel and subjected to air flow of different velocities. The goad of this experiment is to record the sound generated due to air flow past the sheets as well as to measure the air velocity variation after the sheet. By measuring the airflow speed at different locations, it is possible to determine the extents of the boundary later as well as to clarify the generation of eddies.

*Figure 19 WAB Structured Sheet*

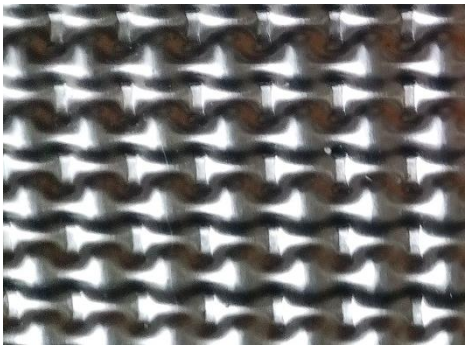

*Figure 20 KMT Structured Sheet*

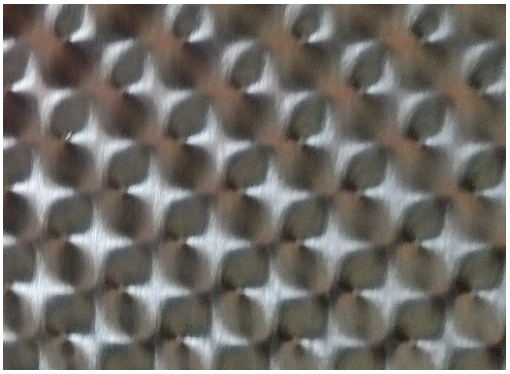

*Figure 21 PWO Structured Sheet*

## 3.1. Experimental Setup

A wind tunnel as shown in Figure 22 was constructed to run up the test. It is composed of a test section of dimensions of 200x150x500 mm connected to an axial ventilator. The ventilator rotational velocity can be set to values from 5 up to 50 Hz. Each sheet specimen was cut into a part of 290x200 mm size. The sheet is placed inside the tunnel test section at mid height of the section wall as shown in Figure 23. The tunnel has holes that can be used to place a hot wire anemometer before and after the test section. A hot wire anemometer coupled with Almemo 2890-9 Data Logger was used to track the velocity fluctuations.

Finally, A Brüel & Kjær type 2250 microphone was mounted above the test section to record the produced sound.

*Figure 22 Experimental Set-up*

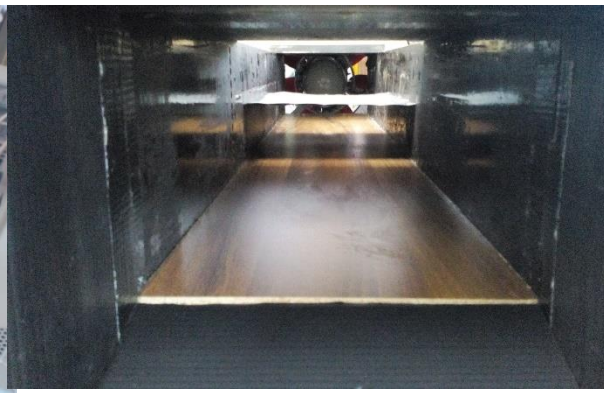

*Figure 23 Sheets placed inside the test section at mid height of the wall*

## 3.2. Methodology:

Each of the three sheets was placed inside the tunnel and tested at different air flow velocities, which is set by different ventilator rotational speed in Hz. For each test case, which is a certain sheet at a certain ventilator speed, the hot wire anemometer was placed before the sheet to measure the inlet velocity at the geometric center of the tunnel profile. Then, the generated sound was recorded at a point $P_m$ which lies on the test section surface above the midpoint of the trailing edge. These recordings are used to obtain the generated sound frequency spectrum.

In addition to the sound measurements, the flow stream-wise velocity above the trailing edge was measured as well. To do that, the hot wire anemometer was placed at four different points, named as $P_1, P_2, P_3\ and\ P_4$, in sequence. These points lie above the trailing edge midpoint at different heights referenced from the sheet surface. The velocity history measured at these points shall be used later to calculate the turbulence intensity at each point. Moreover, a Fast Fourrier Transform, FFT, will be applied to velocity data in order to get the dominating frequency of the generated eddies. The FFT of velocity values used a Hanning window and was performed by a MatLab code that can be found in appendix A. Figure 24 provides a schematic diagram of the front view of the test section clarifying the different measurement locations while Table 3 clarifies the height of each point from the sheet surface.

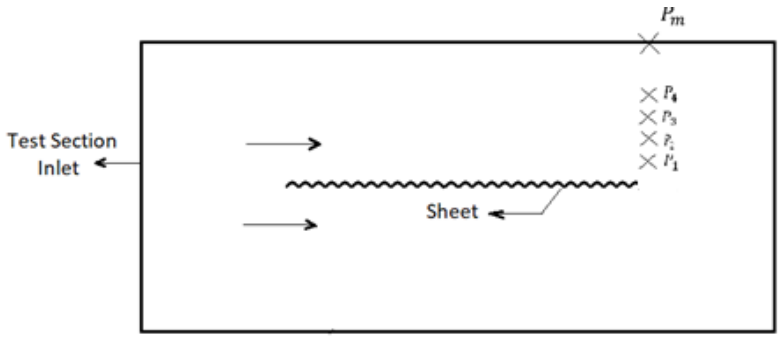


*Figure 24 Schematic Diagram of the Front View of the Wind Tunnel Test Section*

*Table 3 Locations of Measurement Points relative to the sheet*

| Point | Distance from the sheet surface (mm) |
|---|---|
| $P_1$ | 10 |
| $P_2$ | 20 |
| $P_3$ | 30 |
| $P_4$ | 40 |
| $P_m$ | 85 |

It is worth mentioning that this wind tunnel, being operated by an axial ventilator, would act itself as a source of sound. Therefore, the sound measurements obtained from the sheet tests cannot be used directly as they will be biased by a factor equal to the ventilator noise. So to remove this bias, it was necessary to estimate the sound that is attributed to the ventilator only. To do that, sound measurements were performed for the wind tunnel operating with no sheets inside, referred to later as No-Sheet Case. By performing this measurement at each of the ventilator speeds that were used in the tests of sheets, it was possible to have a form of a correction factor that represents the SPL of the sound generated by the ventilator only at each frequency band. By deducting this factor from the measurements of the sheet at the same frequency band, it would be possible to get the SPL due to the airflow only.

However, since the measurements give value of SPL, it would be mandatory to deduce the values of sound power first. Then, the power of the No-Sheet Case is subtracted from the power of the sheet case.

Finally, an SPL is calculated based on the subtraction result. This can be done according to equation 17. Figure 25 shows the frequency spectrum obtained from the No-Sheet Case experiment. It is worth mentioning that from now on, any reference to experimental acoustic results for sheets, would refer to the results after removing the ventilator noise.

$$SPL = 10 * \log(10^{\frac{SPL_{sheet}}{10}} - 10^{\frac{SPL_{no\ sheet}}{10}}) \quad (17)$$

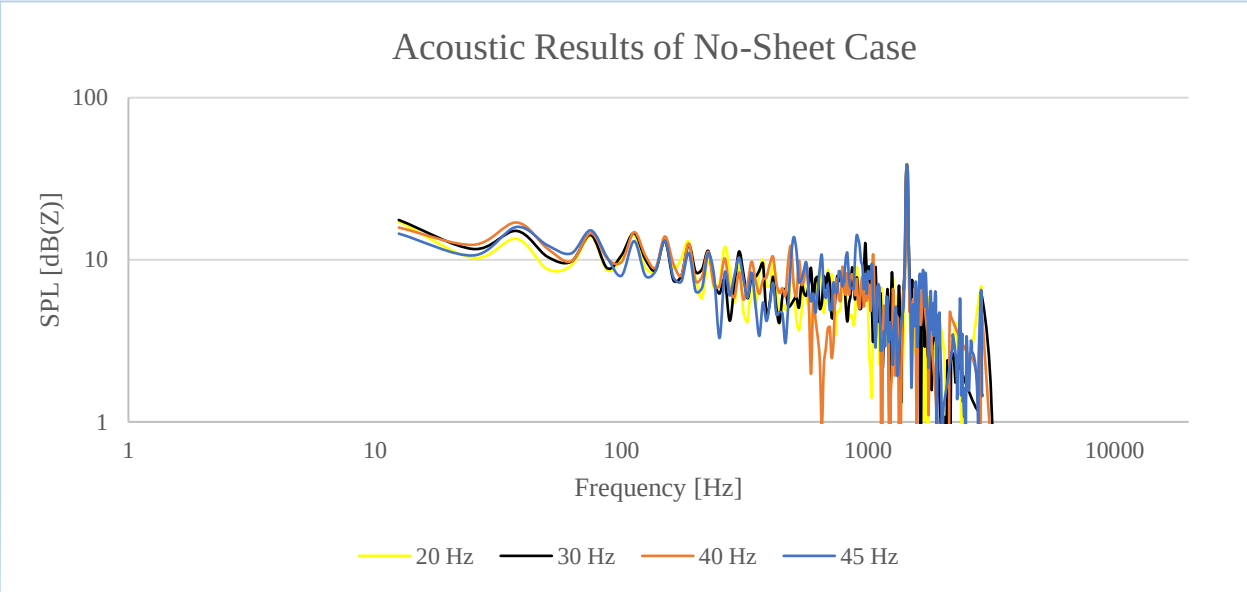


*Figure 25 Frequency Spectrum in case of no sheet inside the tunnel.*

## 3.3. Results:

### 3.3.1. Acoustic Measurements:

Figures (27- 28) show the obtained SPL generated from each sheet, after removing ventilator noise, at different operating speeds. The inlet air velocity ranges from 9 up to 19 m/s. From these figures, it can be noticed the following:

- The highest noise lies in the lower frequency range for all cases for all sheets. This makes sense since with nature of aero-dynamic sound.
- For sheets PWO and WAB, the noise level drops below the human ear ability at frequency above 4 KHz. For sheet KMT, the noise drops starting at frequency 2 KHz.

- Starting from 4 KHz, there is peak behavior at the higher frequency range for sheets WAB and PWO. On the other hand, KMT has a tonal noise generated at frequency of 1450 as well as a wide broadband noise at 950 Hz.
- The level of noise tends to grow in general by increasing the inlet air speed, which is again was expected.

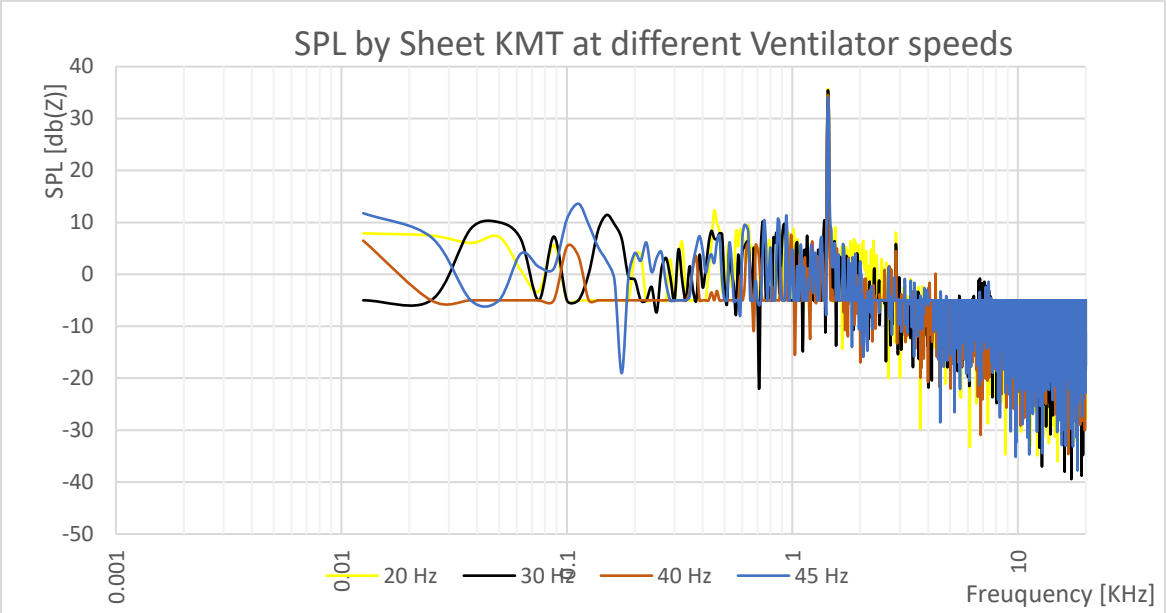


*Figure 27 SPL produced by sheet KMT*

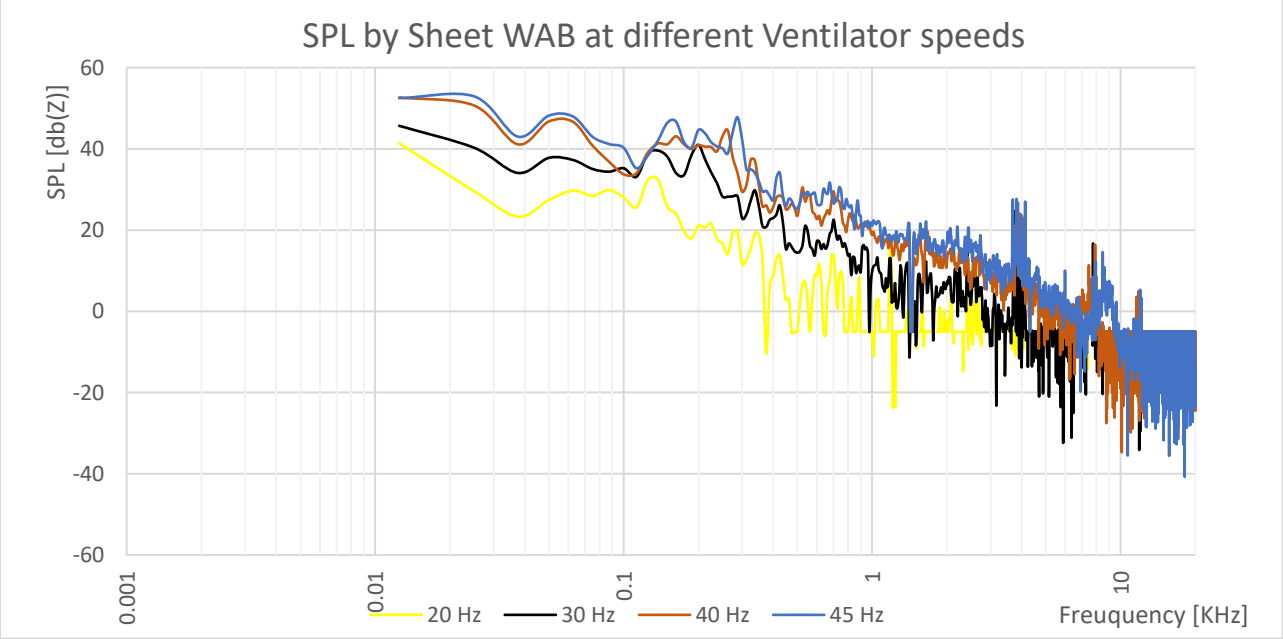


*Figure 26 SPL produced by sheet WAB*

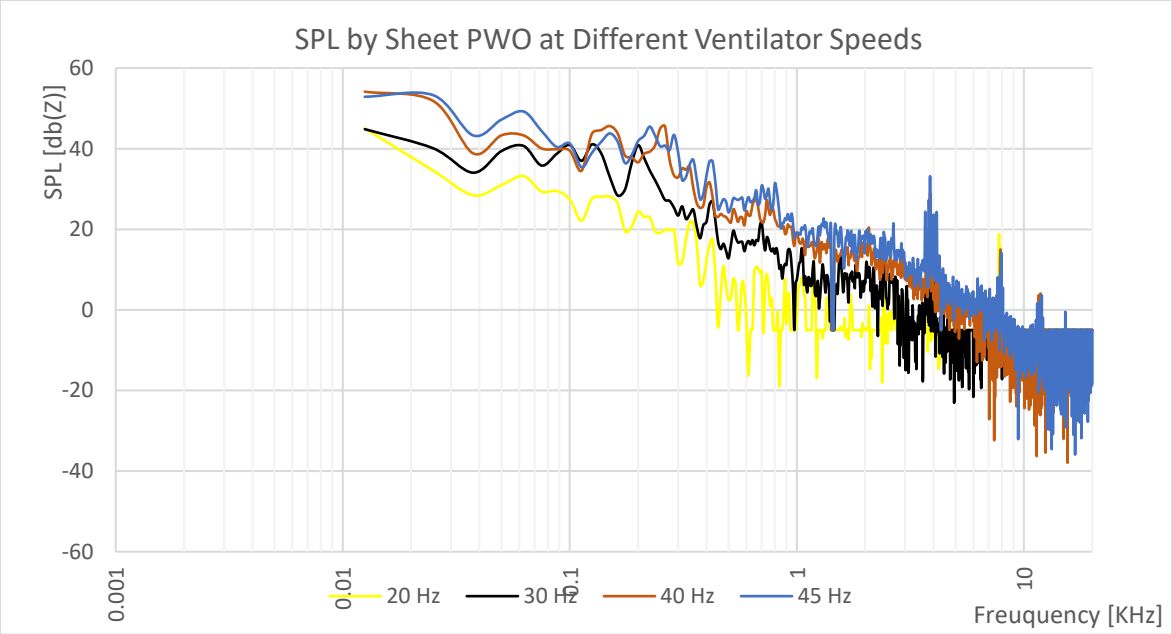


*Figure 28 SPL produced by sheet PWO*

In order to compare between performances of different sheets, figures (29 -32) were plotted showing the performance of different sheets at the same speed. From these figures, it can be noticed that KMT in general produces the least noise.

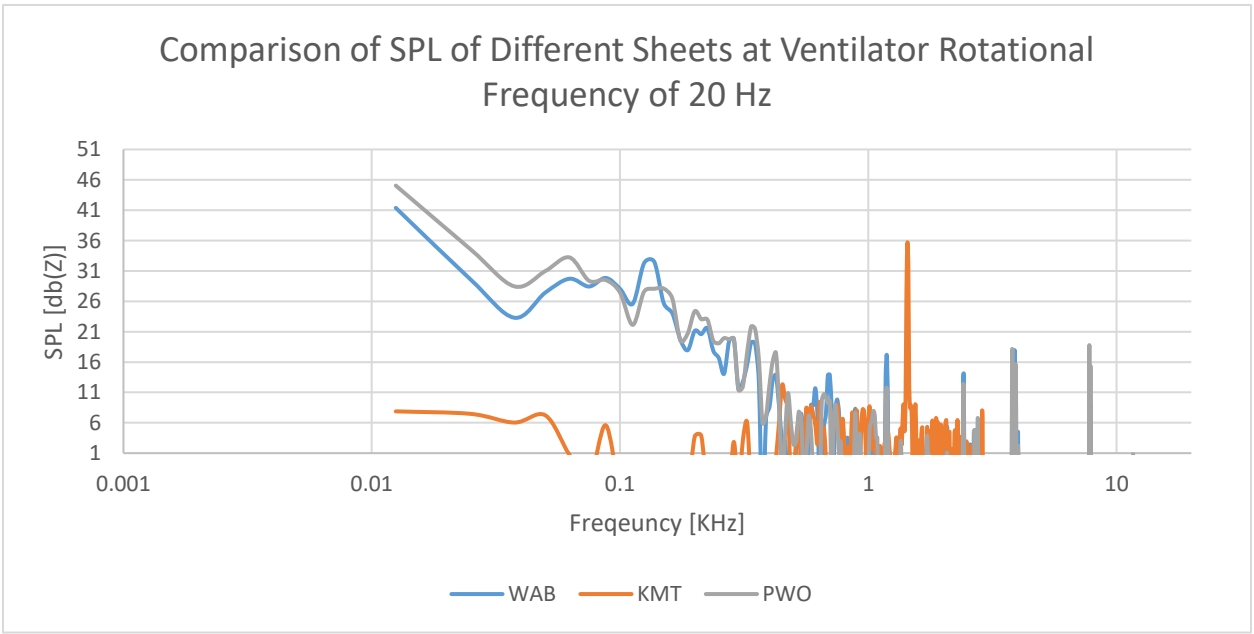


*Figure 29 Comparison of SPL of Different Sheets at Ventilator Rotational Frequency of 20 Hz*

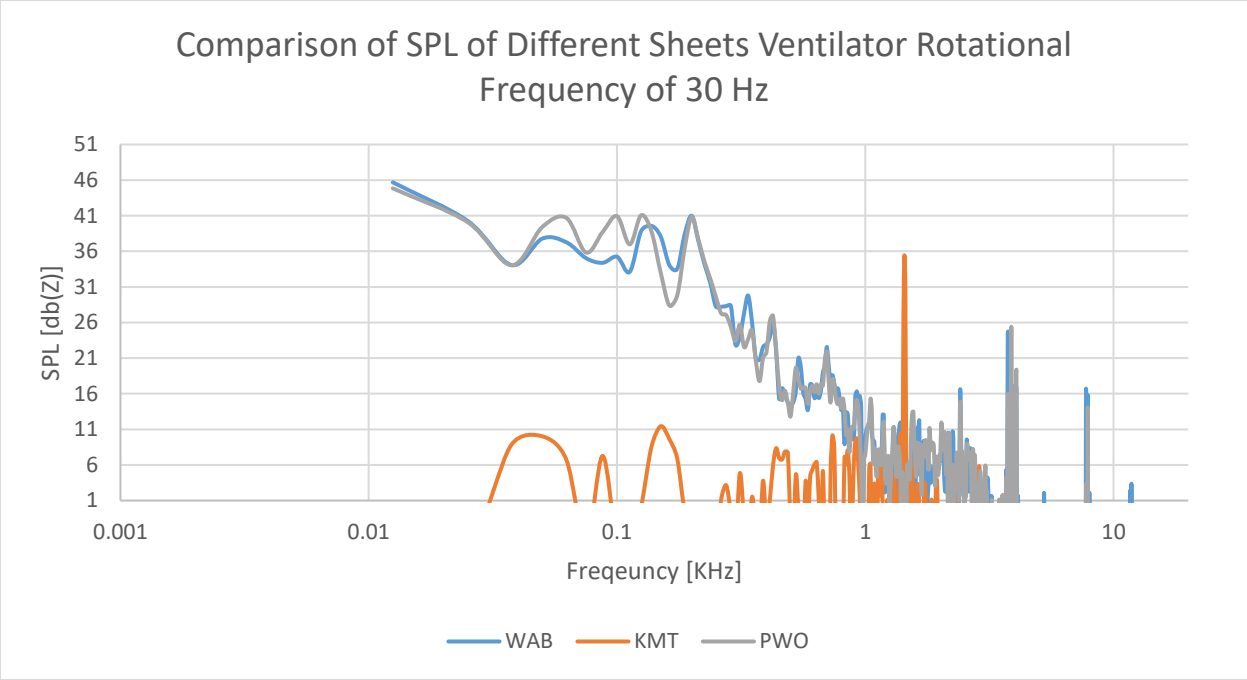


*Figure 30 Comparison of SPL of Different Sheets at Ventilator Rotational Frequency of 30 Hz*

.

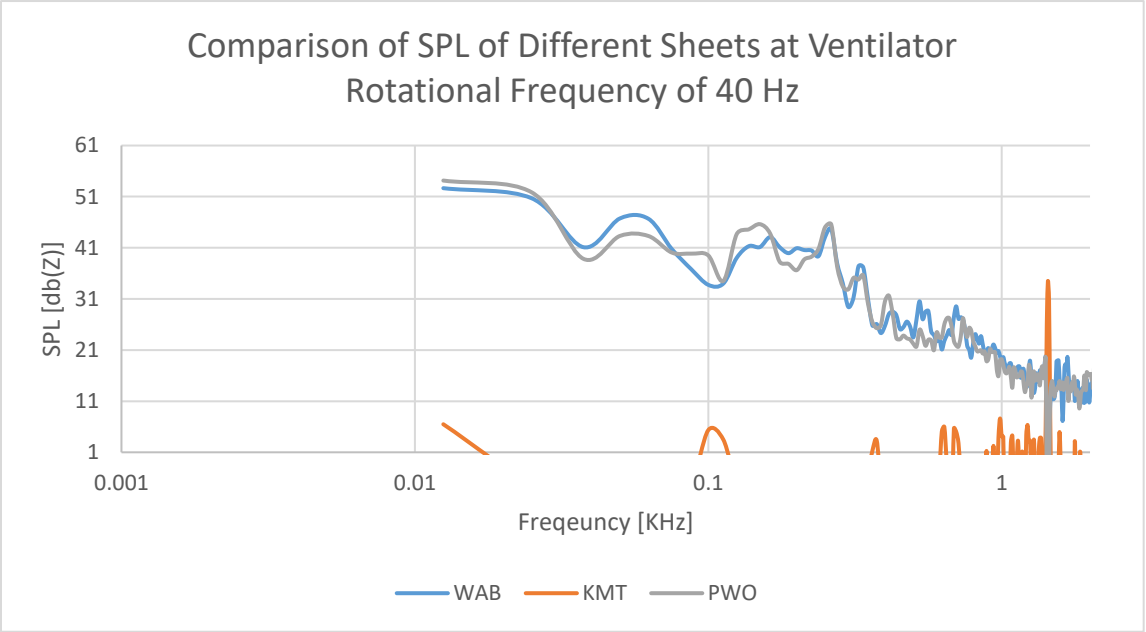


*Figure 31 Comparison of SPL of Different Sheets at Ventilator Rotational Frequency of 40 Hz*

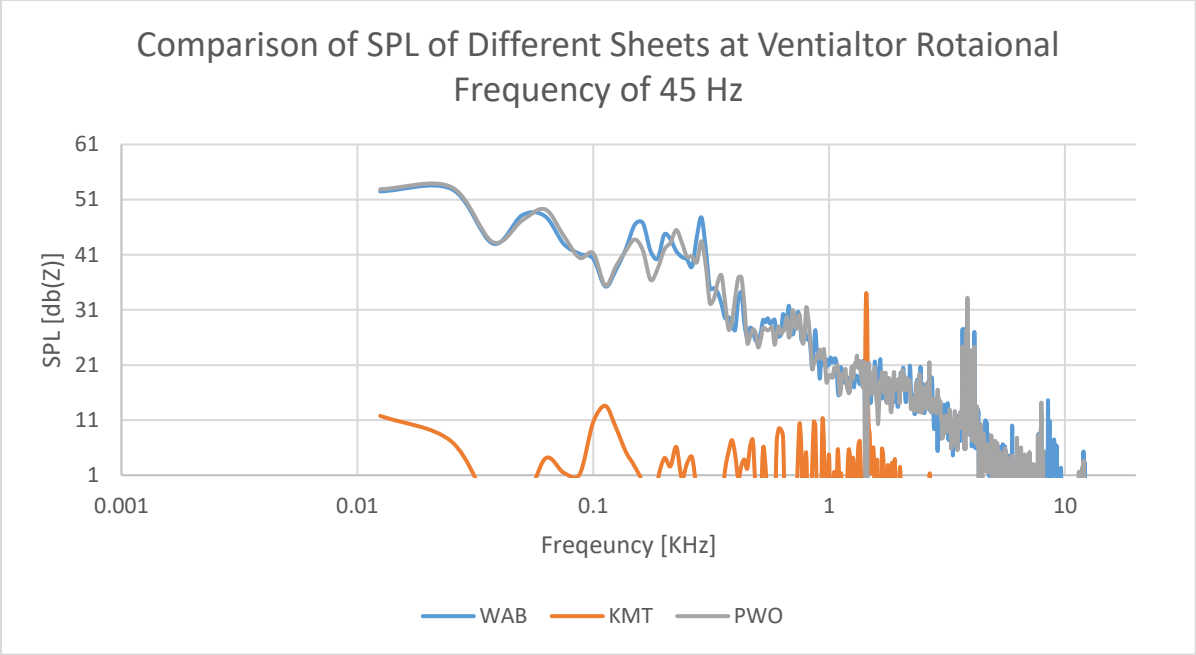


*Figure 32 Comparison of SPL of Different Sheets at Ventilator Rotational Frequency of 45 Hz*

### 3.3.2. Velocity Measurements:

As discussed before, the velocity fluctuations were captured at four different points using a hot wire anemometer. These measurement were performed for each sheet at four different operating speeds. Figures (33 - 35) show the obtained behavior for the three sheets at ventilator speed of 45 Hz as an example. It was found that the velocity changes in a harmonic way that differs in its amplitude and frequency from one case to another. Such a fact may indicate to the presence of vortex shedding. Therefore, it was necessary to plot these values in the frequency domain rather than the time domain. A Matlab code, can be found in Appendix (A), was compiled to perform Fast Fourier Transform to the velocity data. Figures (36 -38) show the velocity in the frequency domain for the three sheets at speed of 45 Hz while figures (70-81) in Appendix (B) show the other cases. From this set of figures it can be noticed that:-

- The further from the sheet it is, the weaker vortex shedding phenomenon is. This can be expected as the flow is no longer affected by sheet texture.
- Sheet PWO has the strongest velocity fluctuations followed by KMT followed by WAB.

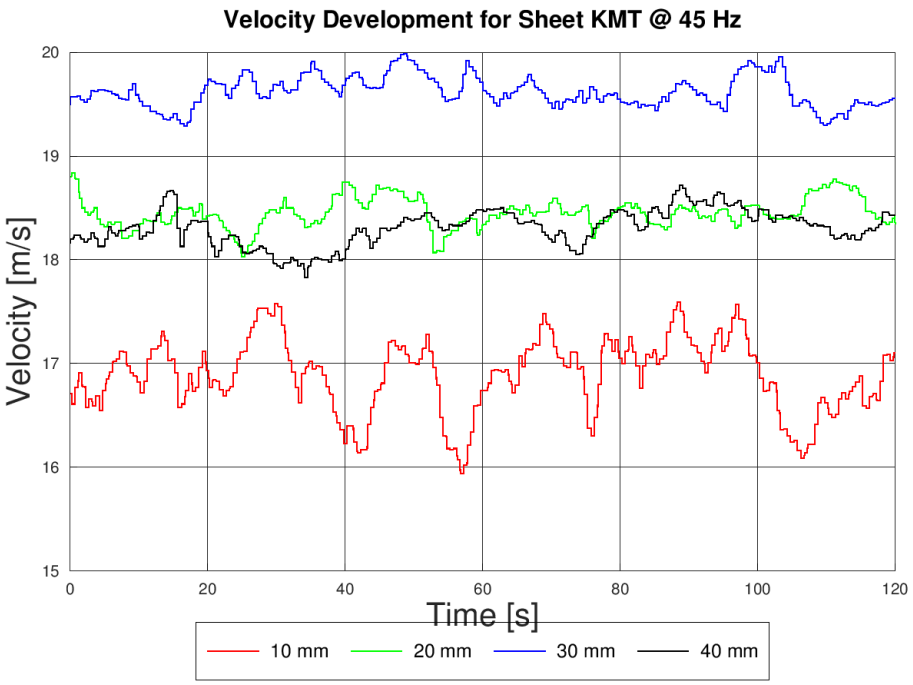


*Figure 33 Velocity Development for Sheet KMT over time at speed of 45 Hz (Average Inlet Air Speed of 20 m/s)*

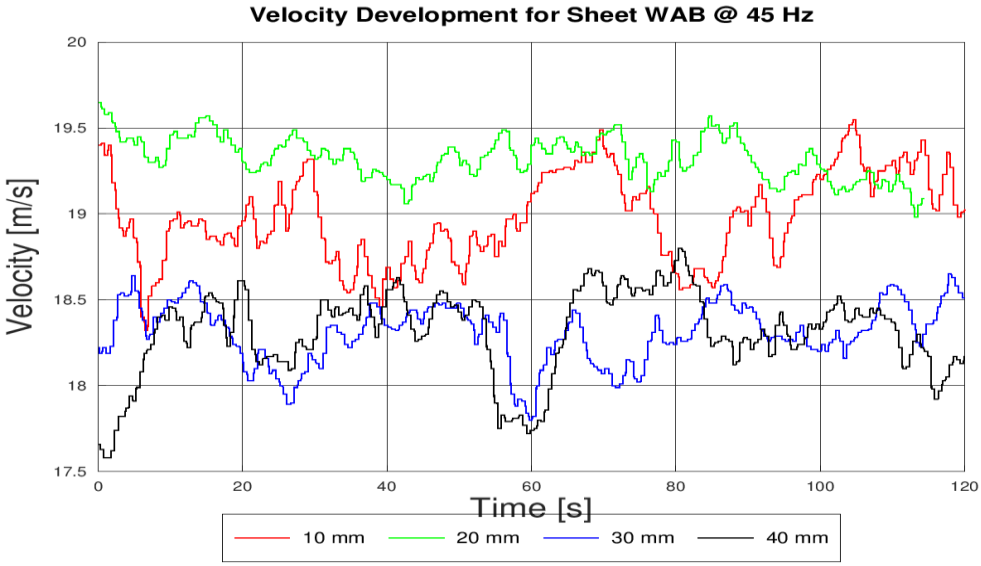


*Figure 34 Velocity Development for Sheet WAB over time at speed of 45 Hz (Average Inlet Air Speed of 17m/s)*

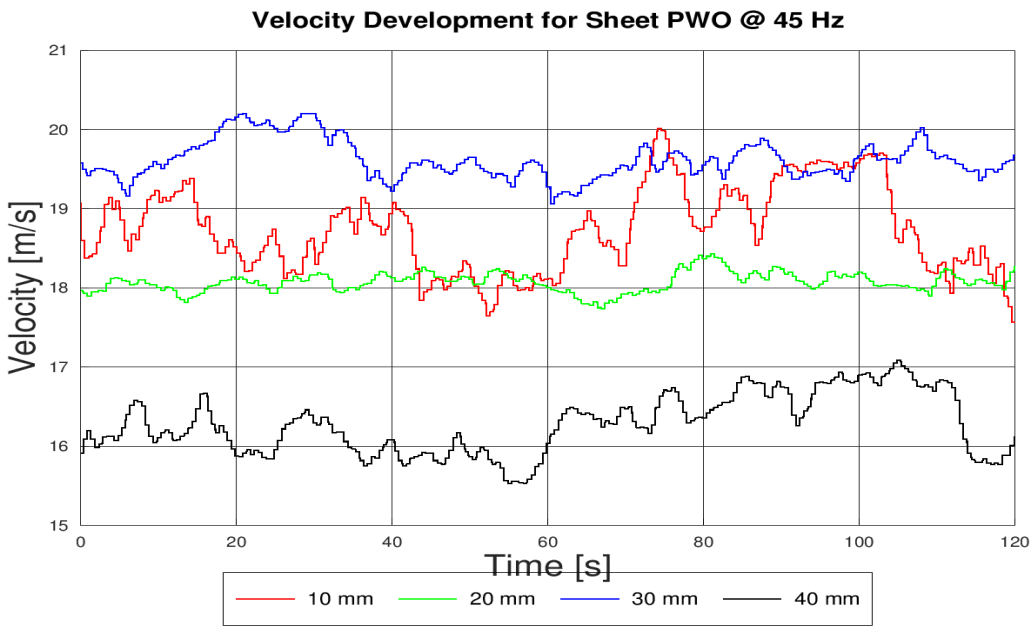


*Figure 35 Velocity Development for Sheet PWO over time at speed of 45 Hz (Average Inlet Air Speed of 19 m/s)*

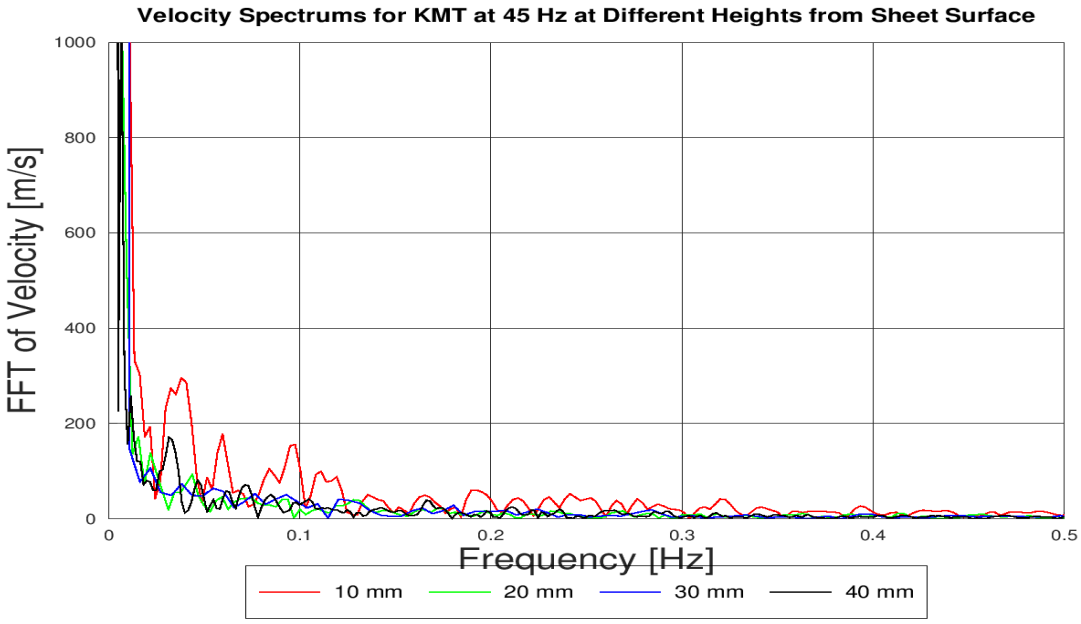


*Figure 36 Spectrum for velocities at different heights at 45 Hz for KMT sheet (Average Inlet Air Speed of 20 m/s)*

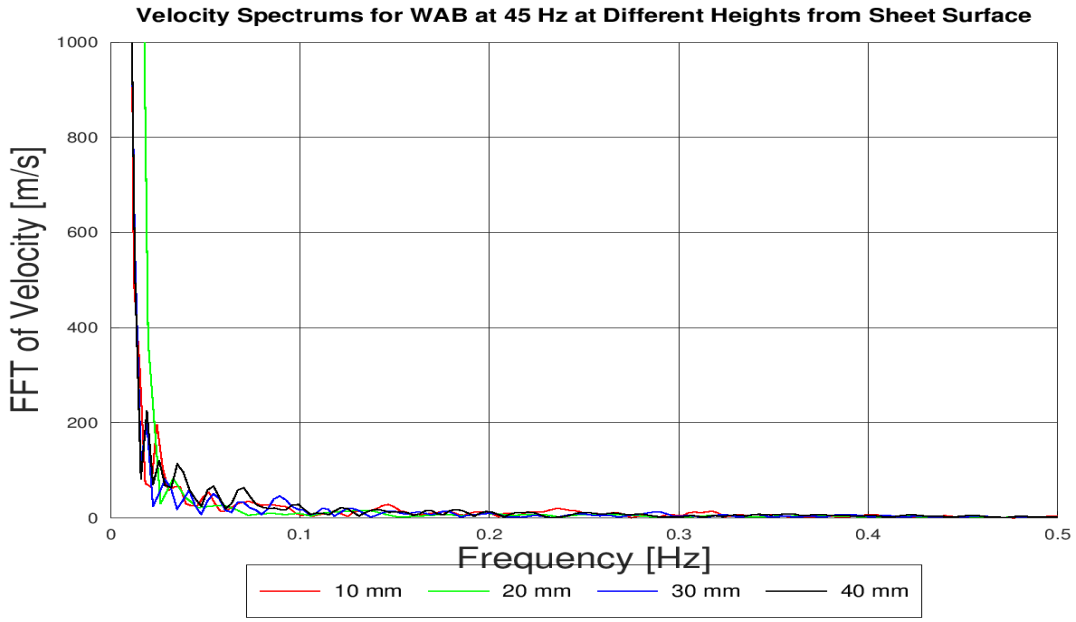


*Figure 37 Spectrum for velocities at different heights at 45 Hz for WAB sheet (Average Inlet Air Speed of 17 m/s)*

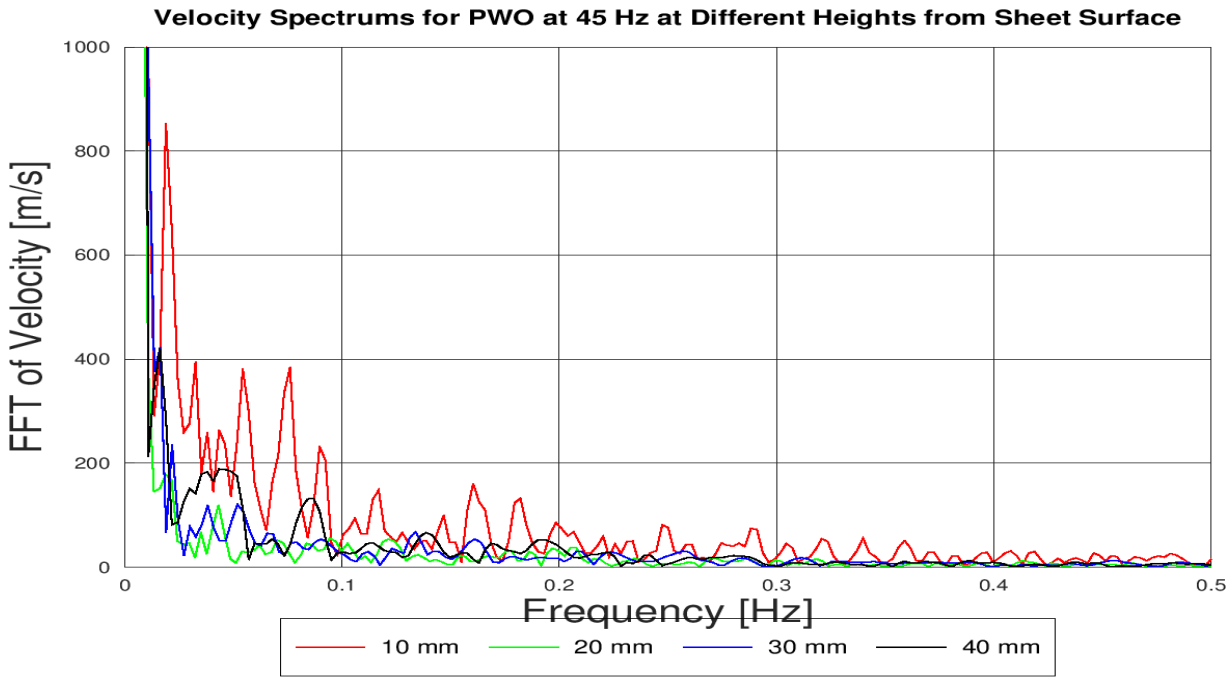


*Figure 38 Spectrum for velocities at different heights at 45 Hz for WAB sheet (Average Inlet Air Speed of 19 m/s)*

Finally, the velocity values presented here were used to calculate turbulence intensity at each case. To investigate the boundary layer generated by each sheet, the mean velocity as well as turbulence intensity were plotted versus the height from the sheet surface in figures ( 39 - 41). By comparing these figures, it can be noticed that:

- Sheet WAB has the smoothest velocity change across height. This was contrary to what was expected since sheet KMT has the least generated sound.
- Sheets PWO achieved the maximum velocity at height of 30 mm. This is the point where the stream is free and is least affected by tunnel ceiling and the sheet texture. On the other hand in case of the WAB sheet, it achieved its maximum velocity at height of 20 mm.

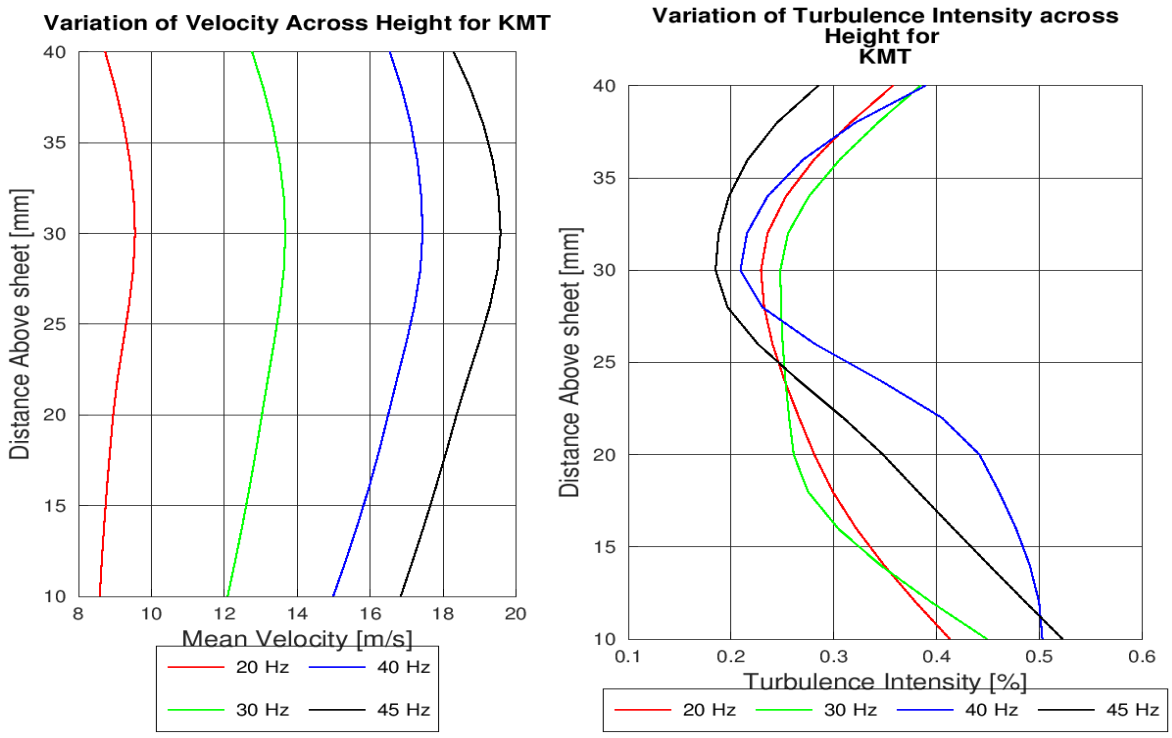


*Figure 39 Boundary Layer Investigation for Sheet KMT*

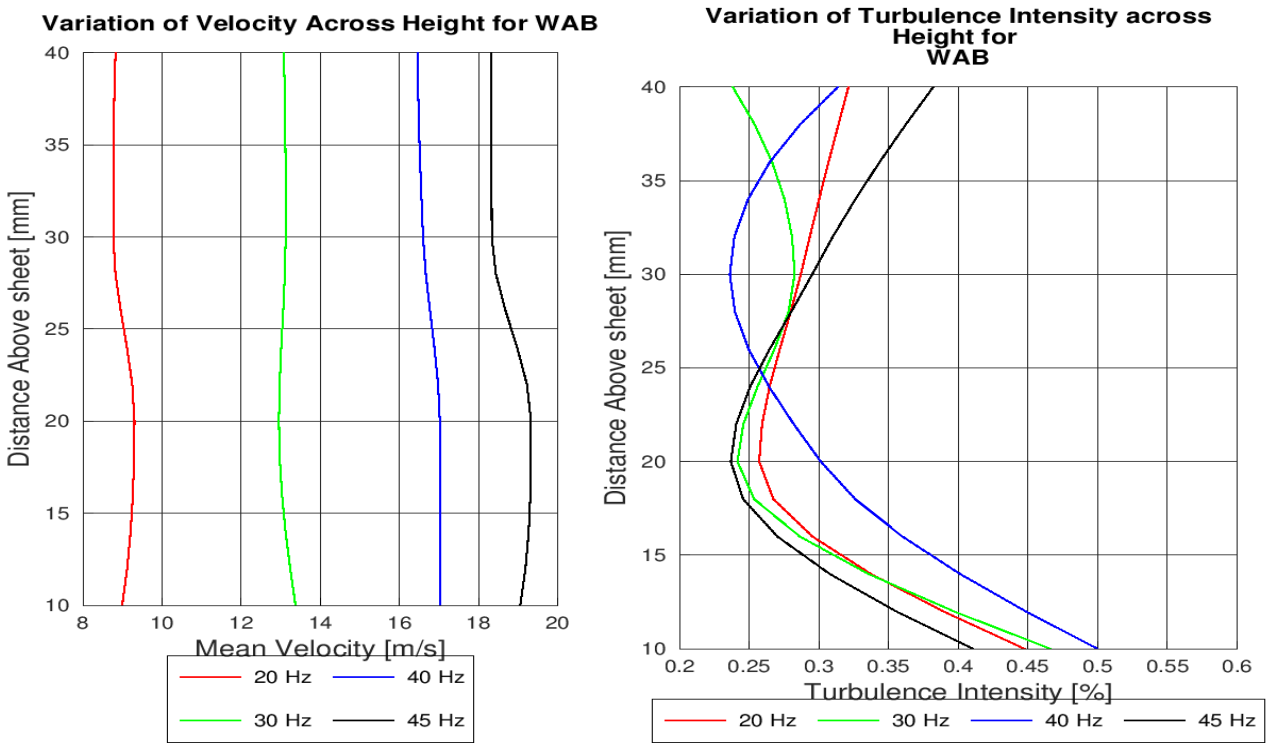


*Figure 40 Boundary Layer Investigation for Sheet WAB*

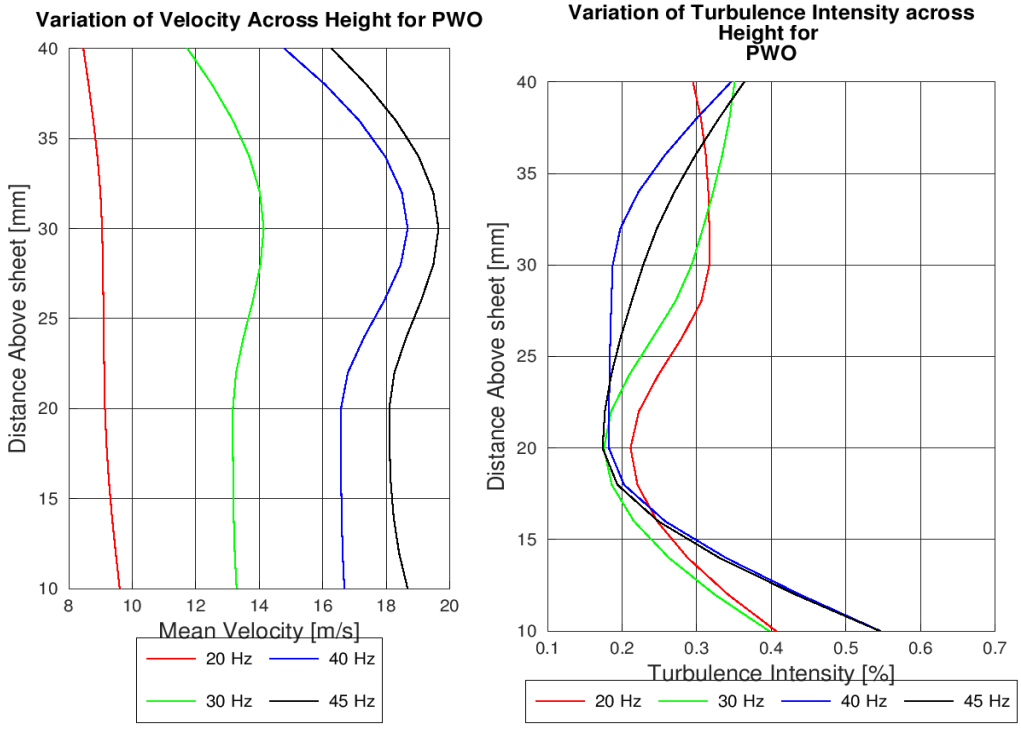


*Figure 41 Boundary Layer Investigation for Sheet PWO*

# 4. Numerical Simulations:

To verify the obtained experimental data, numerical simulation has been done using Ansys Fluent. Due to the complexity and the long time needed for one simulation case, it was only performed for each sheet at the maximum flow speed. The simulation aimed at capturing the transient behavior pf the flow which can be used eventually to estimate the acoustic sources inhibited by presence of the sheet inside the flow. These sources come in the form of a rate of change of pressure on the sheet surface $\frac{dp}{dt}$.

## 4.1. Preparing the Geometry:

The numerical analysis was performed using an electronic version of the sheets where the building unit of each structure pattern was 3D scanned during previous study of the sheets. This building unit was used to build the whole sheet inside Ansys design Modeler. It was impossible to insert the sheet as a whole directly into Ansys fluent due to the limitations inhibited in the software student version over the number of inserted surfaces. Thus, for each sheet, the pattern building unit was inserted into Ansys Design Modeler, as shown in figures 42, 45 and **Error! Reference source not found.**, and patterned in the stream-wise direction as shown in figures 43 , 46 and 49. This leads to a slice-shape models as shown in figures 44 44, **Error! Reference source not found.** and 50. Then, these models are used to represent the fluid domain around the sheet for each case. It is worth mentioning the following points:

- This geometry only models one slice of the sheet. This simplification should be acceptable since this slice is repeated periodically span-wise of the sheet.
- Different parts of the domain would require different meshing strategies. Thus, the fluid domain was divided into two bodies: body (A) which representing the region surrounding the sheet, shown as transparent, and body (B) representing the rest of the domain in grey.
- The model is constructed such that there is enough length for the fluid to develop after leaving the sheet trailing edge. This would be critical to resolving the instabilities in the flow.

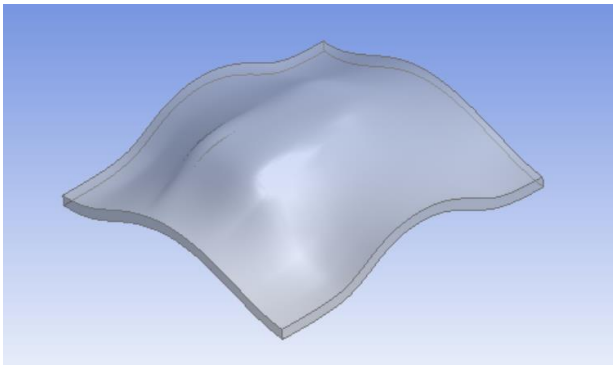

*Figure 42 KMT Sheet Building Unit*

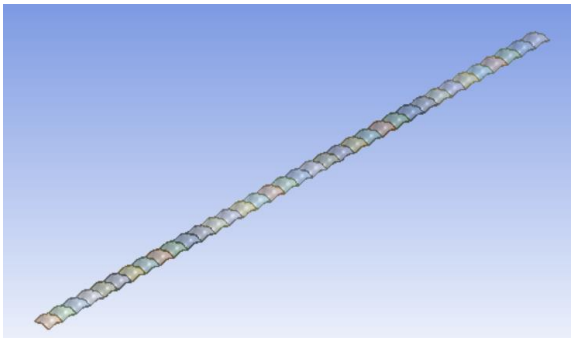

*Figure 43 KMT Sheet Slice*

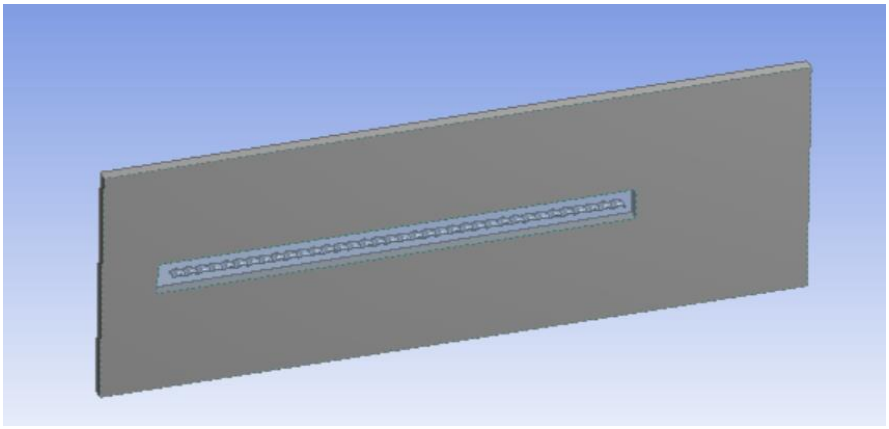

*Figure 44 Fluid Domain for KMT Sheet*

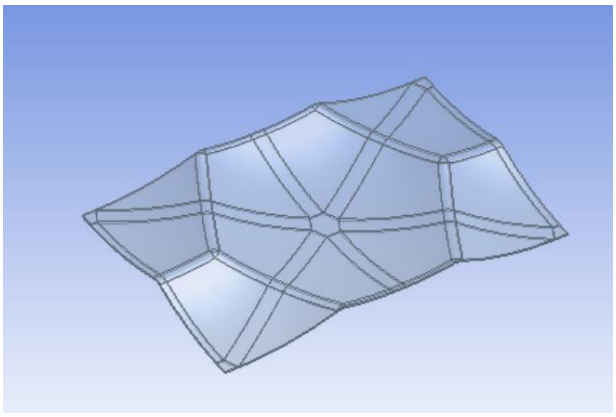

*Figure 45 WAB Sheet Building Unit*

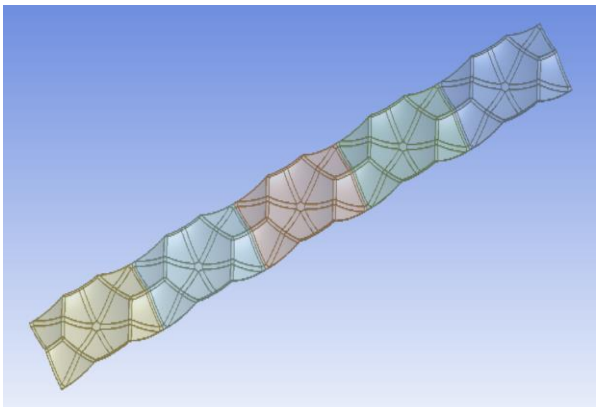

*Figure 46 WAB  Sheet Slice*

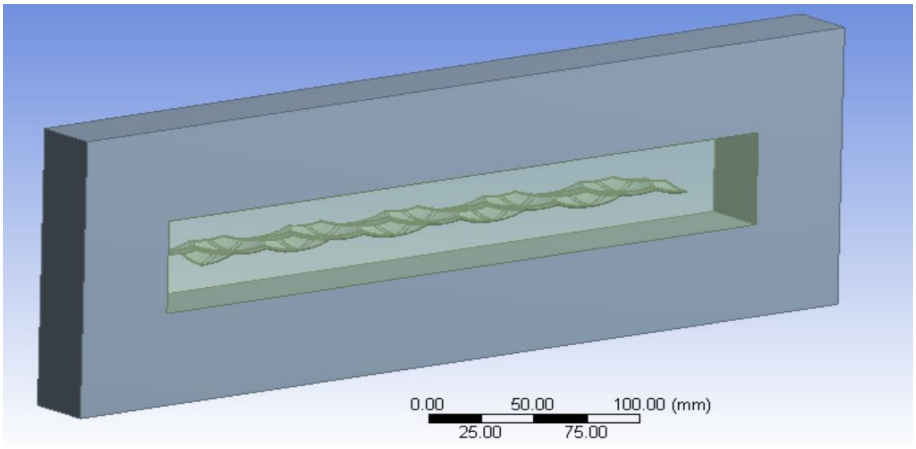


*Figure 47 Fluid Domain for WAB Sheet*

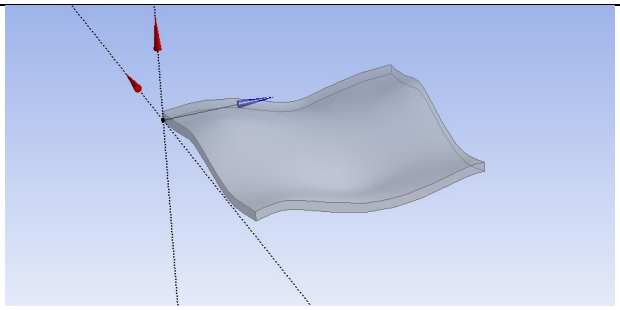

*Figure 48 PWO Sheet Building Unit*

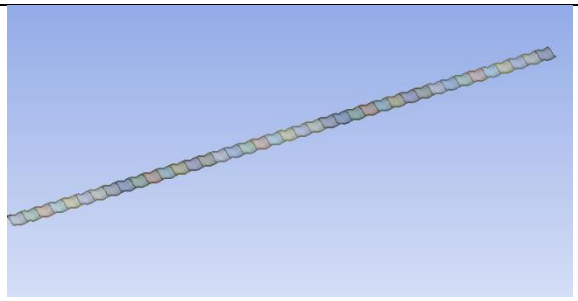

*Figure 49 PWO Sheet Slice*

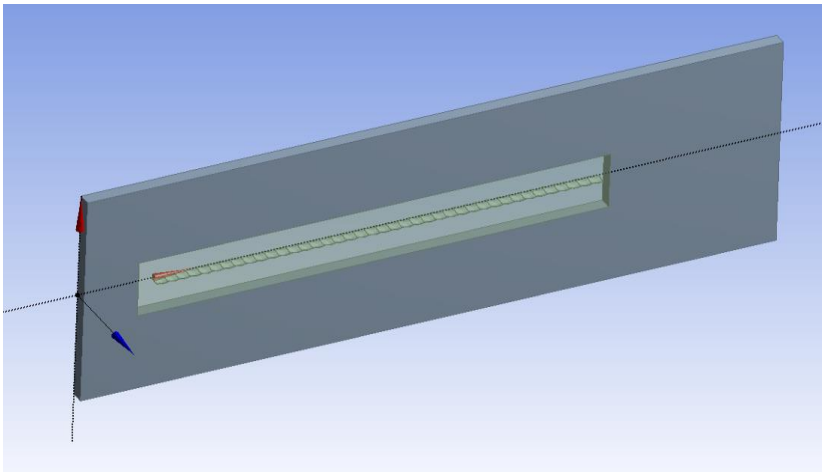

*Figure 50 Fluid Domain for PWO Sheet*

## 4.2. Meshing:

The accuracy of numerical simulation is determined by, among other factors, the quality of the mesh. For these sheets, it was targeted to get the best mesh possible considering the constraints inhibited in the software student version over the number of elements, a maximum of 512 thousands cells. Mesh was mainly built from hex elements using a sweep method. However, the region surrounding the sheet was built from tetrahedron mesh. An inflation layer composed of 10 layers was added at the sheet surface. Table 4, Table 5 and Table 6 clarify the different mesh parameters while, Figure 51, Figure 52 and Figure 53 show the obtained mesh.

### 4.2.1. KMT Case Mesh:

*Table 4 Mesh Parameters for KMT Case*

| Feature | Body | Properties |
|---|---|---|
| Body Sizing (Tetra Hedral) | A | 1 mm size |
| Inflation Layer | A | With maximum of 10 layers and smooth transition option using transition ratio of 0.272 and growth rate of 1.2% |
| Sweep Meshing (Hex Dominant) | B | 3 mm element size |

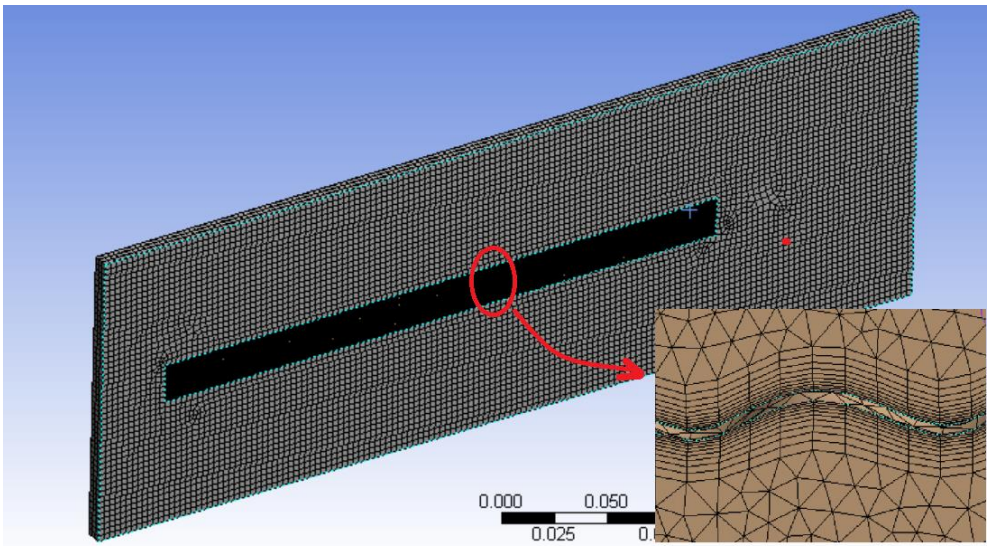


*Figure 51 Mesh of KMT Case*

### 4.2.2. WAB Case Mesh:

*Table 5 WAB Case Mesh Parameters*

| Feature | Body | Properties |
|---|---|---|
| Body Sizing (Tetra Hedrons) | A | 3 mm size |
| Inflation Layer | A | With maximum of 15 layers and total thickness of 1 cm |
| Sweep Meshing (Hex Dominant) | B | 3 mm element size |

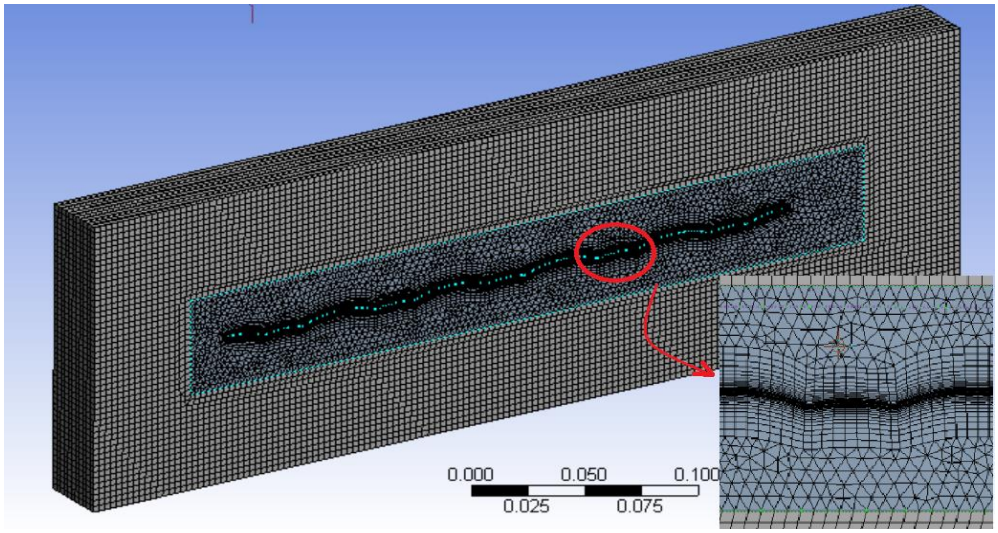


*Figure 52 Mesh for WAB Case*

### 4.2.3. PWO Case Mesh:

*Table 6 WAB Case Mesh Parameters*

| Feature | Body | Properties |
|---|---|---|
| Body Sizing (Tetra Hedrons) | A | 3 mm size |
| Inflation Layer | A | With maximum of 15 layers by smooth transition |
| Sweep Meshing (Hex Dominant) | B | 1.5 mm element size |

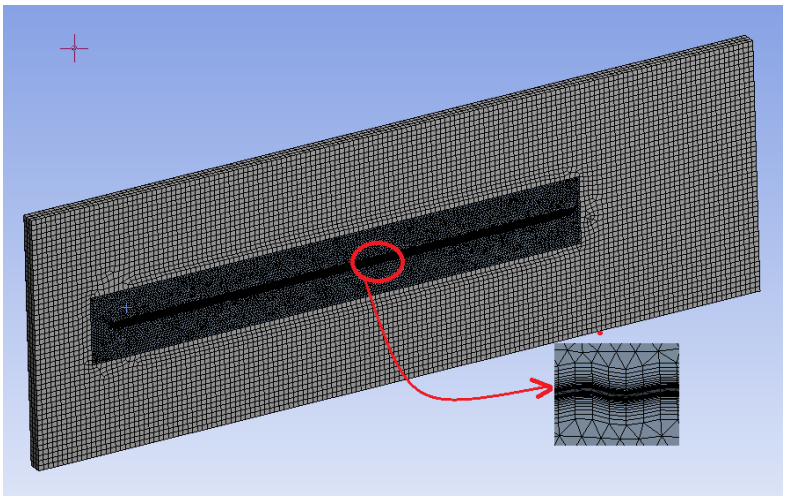

*Figure 53 Mesh for PWO Case*

## 4.3. Case Set-up:

The problem was represented by four boundary conditions shown in Table 7. The boundary conditions were similar for all cases except for the value of inlet velocity.

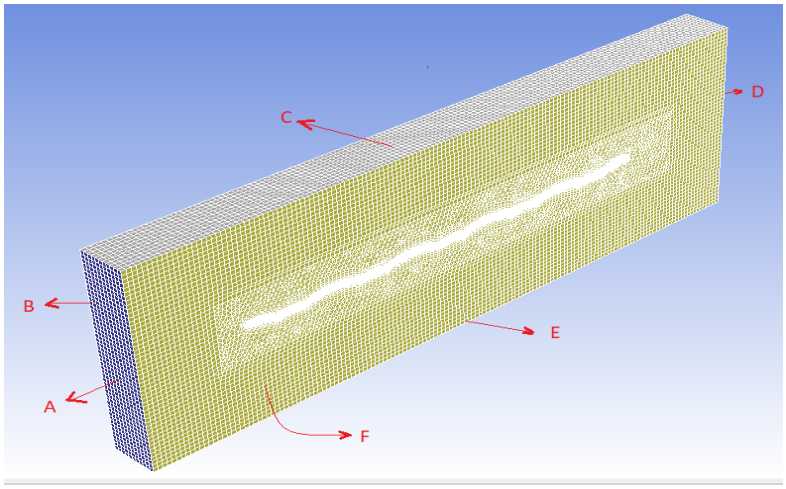


*Figure 54 Boundary Condition Definition*

*Table 7 Boundary Conditions*

| Boundary Condition | Surface |
|---|---|
| Velocity Inlet | A |
| Pressure Outlet | D |
| Wall | C and E |
| Periodic Interface | F and B |

Before starting the transient analysis, the problem has been solved as a steady state case. This was in order to provide a good starting point for the transient analysis. Considering the velocities involved in the problem, < 20 m/s, a pressure based solver was chosen for both cases. For the steady state run, a $k-\omega$ with SST model was used as a viscosity model. Solution method as well discretization schemes were used as shown in Table 8

*Table 8 Steady State-Run Solution Method*

| Item | Property |
|---|---|
| Pressure-Velocity Coupling | SIMPLE Method |
| Gradient Discretization | Green-Gaus Cell Based |
| Pressure Discretization | 2nd Order |
| Momentum Discretization | 2nd Order Upwind |
| Turbulent Kinetic Energy Discretization | 2nd Order Upwind |
| Specific Dissipation Rate Discretization | 2nd Order Upwind |

For the transient run, an LES model with Kinetic Energy Transport as a sub-grid model was used for modelling viscosity. Solution method was selected according to Table 9.

*Table 9 Transient Run Solution Method*

| Item | Property |
|---|---|
| Pressure-Velocity Coupling | PISO |
| Gradient Discretization | Green-Gaus Cell Based |
| Pressure Discretization | 2nd Order |
| Momentum Discretization | Bound Central Differencing |
| Sub-grid Kinetic Energy Discretization | 2nd Order Upwind |
| Transient Formulation | Bound 2nd order implicit with frozen flux formulation |

**Defining a Time Step:**

The problem with simulation of acoustic in particular is that it involves variations on a very wide scale where acoustic pressure fluctuations may be on order of magnitude of $2x10^{-5}$ Pa, the human ear hearing threshold, whereas the flow may have fluctuations on order larger than 1 Pa due to any other phenomena. According to the discussion that was presented before in this report, it was found that LES model is the best candidate as a turbulence model to capture the acoustic behavior of the flow due to its sub-grid options.

However, due to the demanding computation resources required by LES, it is crucial to select an appropriate settings for the transient analysis from the point of view of time step and simulation time. The time step used by the calculation determines the largest frequency that can be captured during the analysis where:

$$f_{max} = \frac{1}{2\,\Delta\,t} \tag{18}$$

where $\Delta\,t$ is the time step. On the other hand, the time duration that is covered by the simulation determines the least captured frequency. Selecting a time step that is small enough to resolve the high frequency spectrum would mean that the simulation needs a lot of time steps to cover time range big enough to resolve the small frequencies [15]. Based on the acoustic results obtained experimentally, it was decided to focus on the range up to 20 KHz. Hence, a time step of 0.000025 second was selected using equation 18 for all the cases.

**Acoustic Analysis:**

The transient analysis was run for 3000 iterations in order for the problem to reach a stable status. Only at this point, the solution starts to be accurate. Therefore, the acoustic module in Ansys is activated in order to calculate the sound sources at the sheet surface. To do that, Ffwocs Williams and Hawkings model is used where a receiver was defined at the same location for the microphone in case of the experiment. However, it is necessary for the receiver point to be inside the fluid domain. Therefore it was defined at a height of 75 mm instead of 85 mm as it was in the experiment.

## 4.4. Numerical Results:

### 4.4.1. Numerical Results of KMT Sheet:

Figure 55 shows the obtained velocity contour at a plane that coincides with the model mid-plane. From this figure, it can be noticed that the simulation has managed to capture the formed eddies. However, some error can be noticed at the boundaries of body A. This may be accounted to the jump in mesh size in this area. Unfortunately, it was hard under the student version constraints to use better mesh for this sheet geometry.

On the other hand, it can be noticed how the boundary layer develops across the sheet length from laminar to turbulent. It is worth mentioning that this transition occurs at the twentieth structure unit which is at a distance of 16 cm from the sheet leading edge. Figure 56 shows the velocity vectors at the point at which the boundary layer transitions from laminar to turbulent.

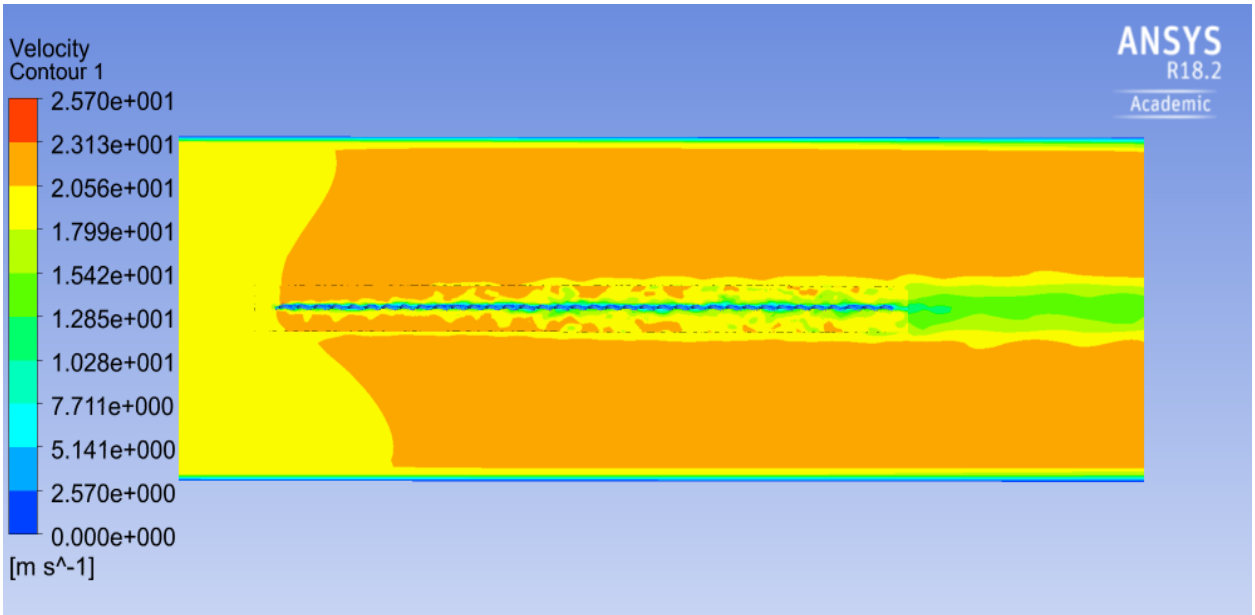


*Figure 55 Velocity Contour at KMT sheet Mid-Plane*

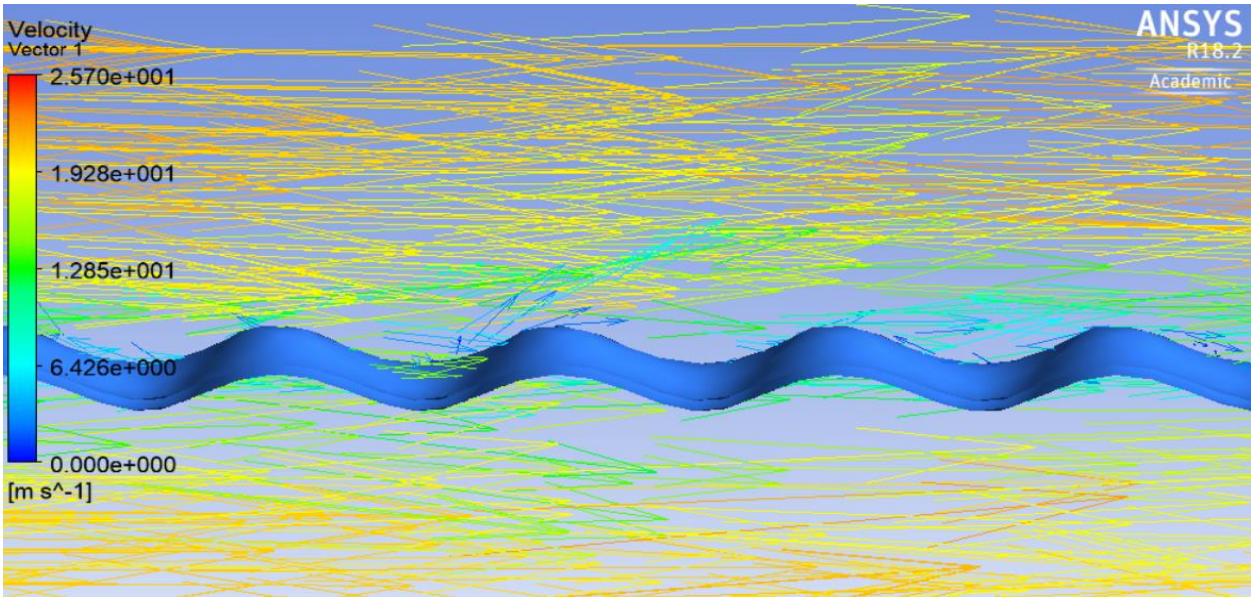


*Figure 56 Velocity Vector at Transition point from laminar to turbulent for KMT Sheet*

### 4.4.2. Numerical Results of WAB Sheet:

Figure 57 shows the obtained velocity contour for the WAB sheet where it can be noticed that:

- Thanks to the more uniform geometry of the WAB sheet than the KMT sheet, it was possible to construct a more uniform mesh. This small and uniform mesh enabled the LES model to capture the flow behavior better than the case with the KMT sheet.
- Like sheet KMT, the flow has eddies formed over the sheet length and a wake region is generated.
- The boundary layer again transforms from laminar to turbulent. However, the transition here happens much earlier than with the KMT sheet where it occurred after passing by one structure unit which means after traveling 6 cm over the sheet length in contrary to 16 cm with KMT sheet.

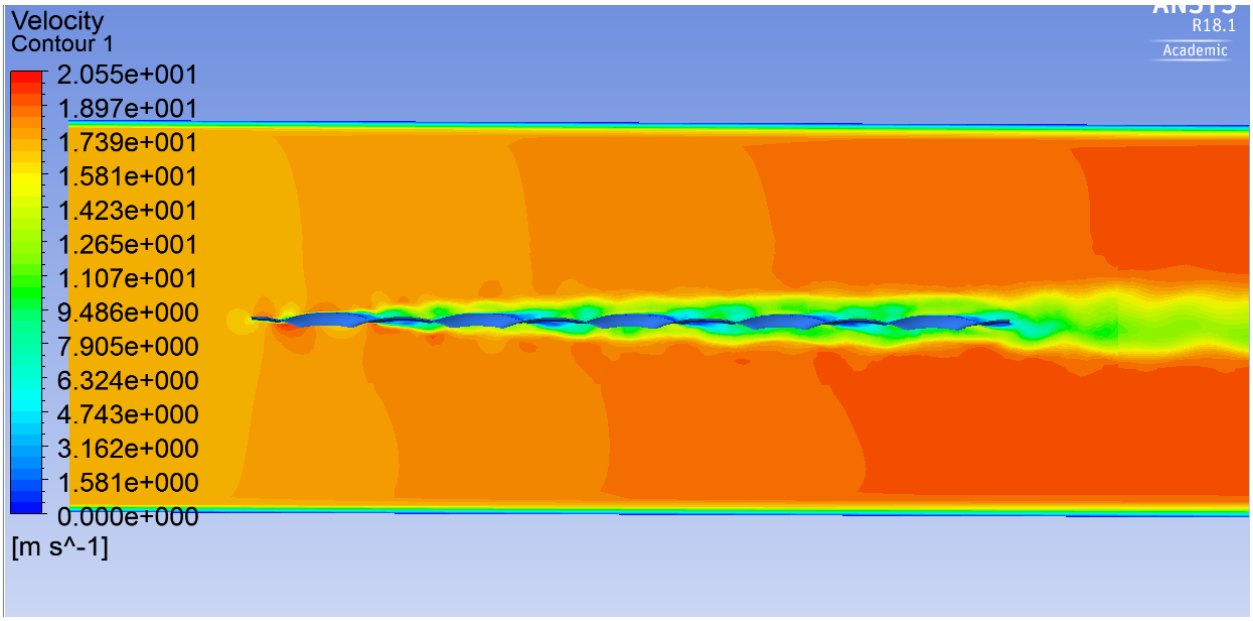


*Figure 57 Velocity Contour at WAB sheet at the mid-Plane*

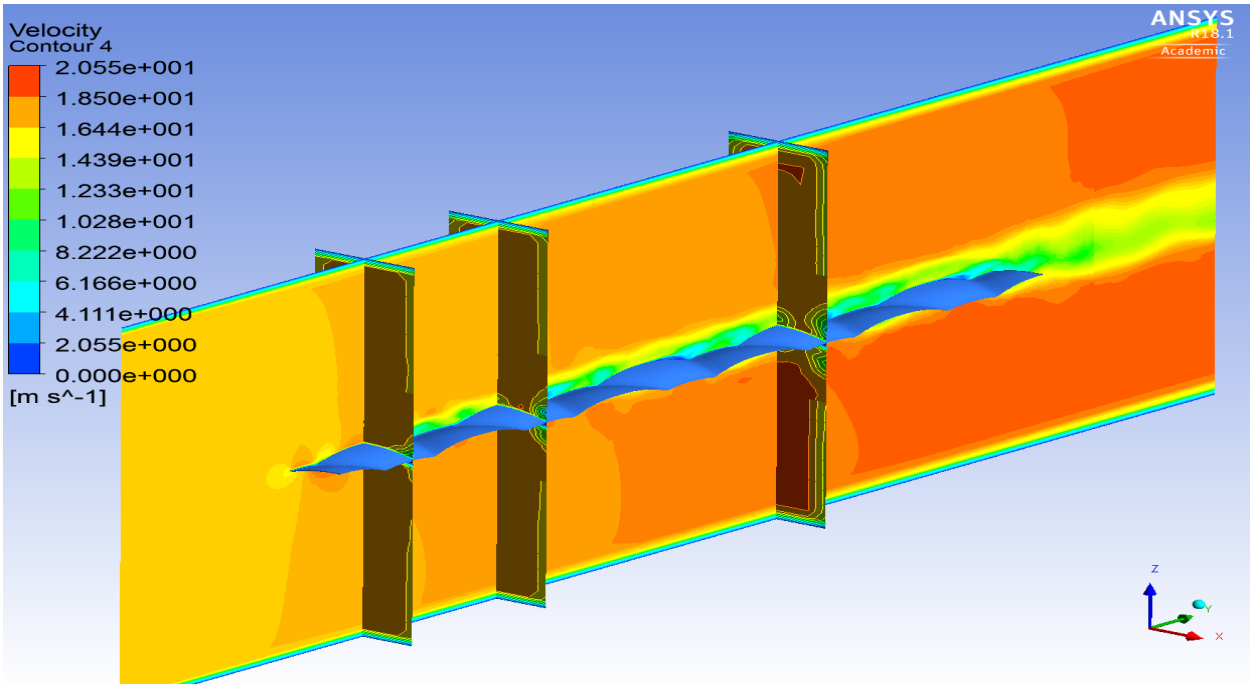


*Figure 58 the Eddies of WAB in 3D*

### 4.4.3. Numerical Results of PWO Sheet:

Figure 59 shows the velocity contour at the mid-plane of sheet PWO. Like the other two simulation, eddies can be seen formed around the sheet surface. From these two figures, it can be noticed that:

- Like the other sheet, the fluid transitions from laminar to turbulent.
- Similar to KMT sheet, the laminar section length is relatively long, both sheets have long laminar section compared to the WAB sheet.
- A problem can be seen in the results after the sheet trailing edge similar to that in the KMT sheet. Again this problem arises because of the rough transition in mesh from fine to coarse at the boundaries of body A.

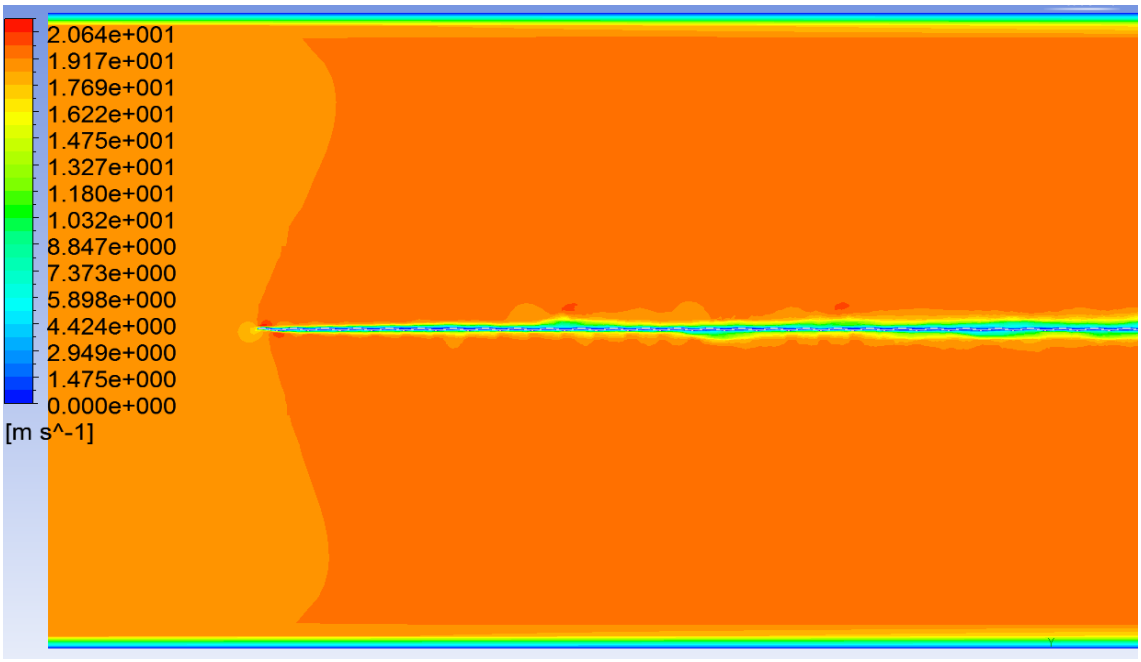


*Figure 59 Velocity Contour at PWO sheet Mid-Plane*

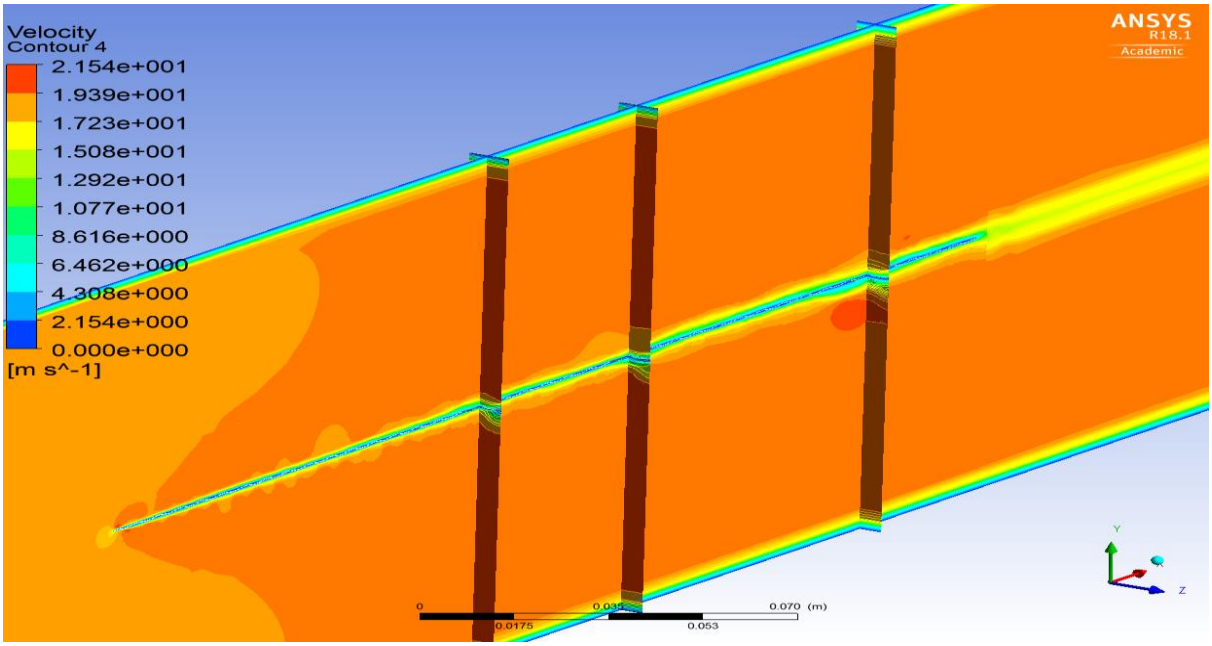


*Figure 60 The eddies  of PWO in 3D*

## 4.5. Comparing Numerical and Experimental Results:

### 4.5.1. Comparison of acoustic Results:

By comparing the acoustic results obtained from simulation and experiment in figures (61 -63), it can be noticed that the two approaches agree on the general trend of SPL in some frequency ranges and disagree in others. A cases for disagreement came in a way such that the experimental data was higher than the numerical in form of peak noise or broad band noise, or both together. An example for that is the PWO sheet in Figure 62 in the frequency range above 500 Hz and for WAB sheet in figure 61 all over the scale. This most probably refers to external noise imposed on the experimental measurements. It is worth considering the fact that the experimental results are based on two measurements: once with the sheet and once without. Therefore, it is more likely to inherit more sources of error.

- On the other hand, in Figure 61 which shows the data of WAB sheet, which is the case with the best mesh, we can find perfect similarity in the trend in the range of 13 up to 70 Hz.

- KMT sheet in Figure 63 has a different case where the numerical data were higher than experimental one. Taking into consideration that KMT had the most problems with velocity contours, which indicates it is the worst mesh, it can be concluded that the numerical data overestimated the generated noise, although we can still find some similarities in the two trends.

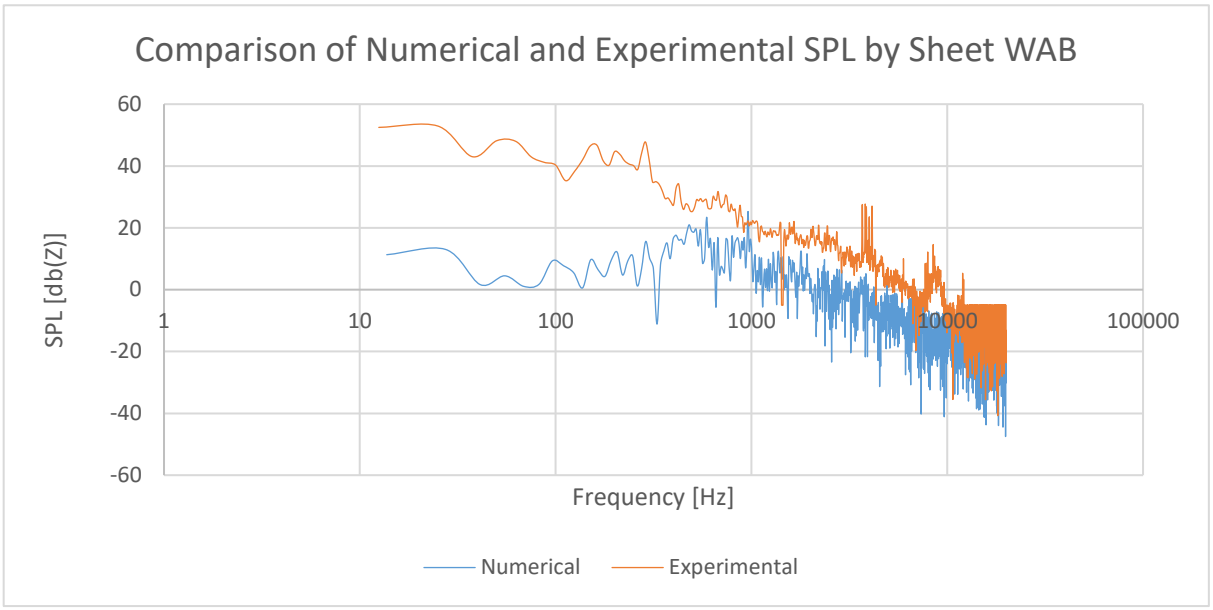


*Figure 61 Comparison of Numerical and Experimental Acoustic Results for WAB*

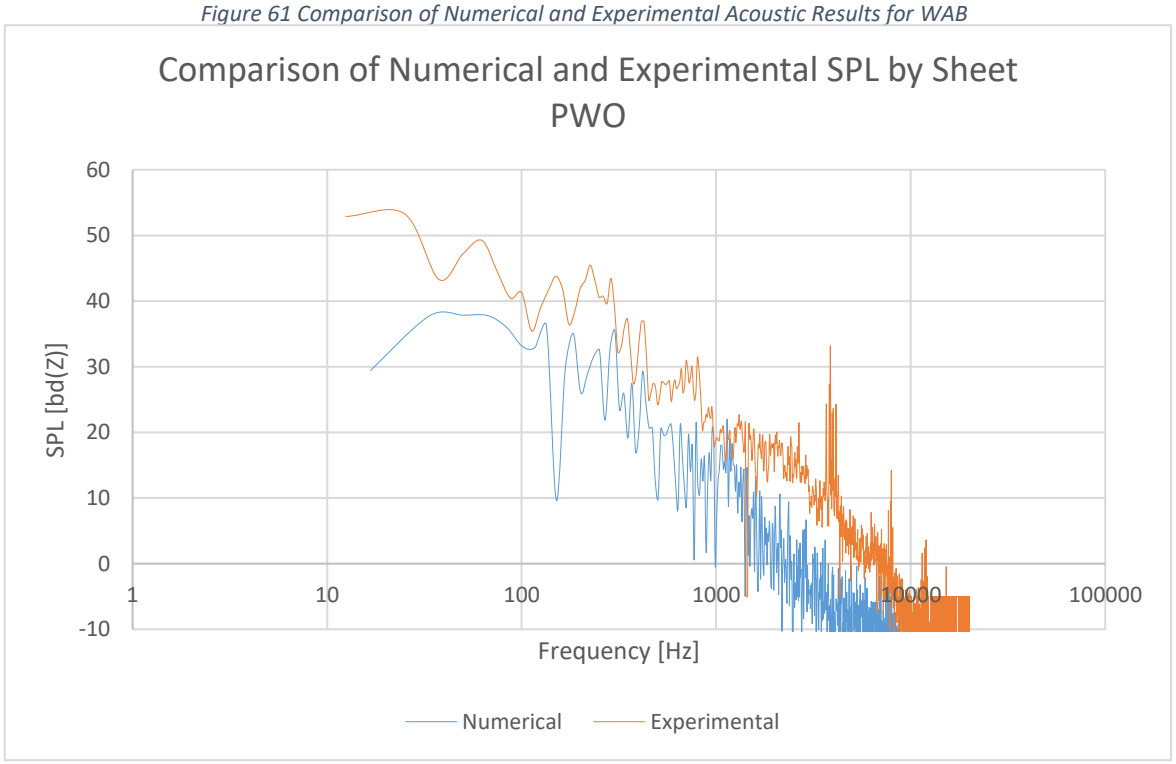


*Figure 62 Comparison of Numerical and Experimental Acoustic Results for PWO*

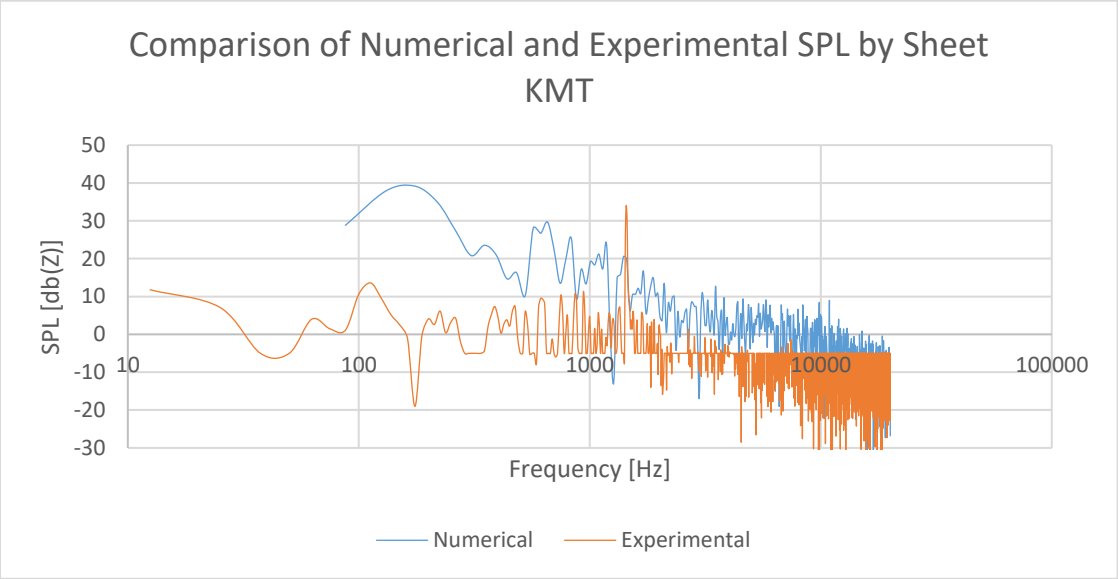


*Figure 63 Comparison of Numerical and Experimental Acoustic Results for KMT*

### 4.5.2. Comparing Numerical to Experimental Velocity and Turbulence Intensity:

Figures (64- 69) compare velocity and turbulence intensity obtained from the two approaches: experimental and numerical. In these figures, each of velocity, turbulence intensity as well as their respective error is plotted versus the height from the sheet. The velocity and turbulence intensity are plotted on lower horizontal axis while the error percentage between the two approaches is plotted on the upper axis. From these figures, it can be noticed the following:

- The two approaches agree, to some extent, in the trend of velocity across height for sheets KMT and WAB in figures 64 and 66 respectively. However, it disagrees for sheet PWO in Figure 68.
- Sheet PWO has the least velocity error, 0.06%, however since this sheet has problems with agreement in velocity trend between the two approaches, this result is not reliable. Comes next to the PWO is the WAB sheet with error ranging from 2.3% to 43 %. Taking into consideration it was the sheet of best mesh, this result makes sense.
- Regarding turbulence intensity, it is clear that it has generally much higher error. This may be returned to the fact that the two approaches have different time scales where the hot wire anemometer measures velocity value once per 0.07 seconds. On the other hand, the simulation runs with a time step of 2.5E-5 seconds, to meet convergence

criteria. This difference in time scales would imply error in a quantity like turbulence intensity that depends on averaging a certain number of value.

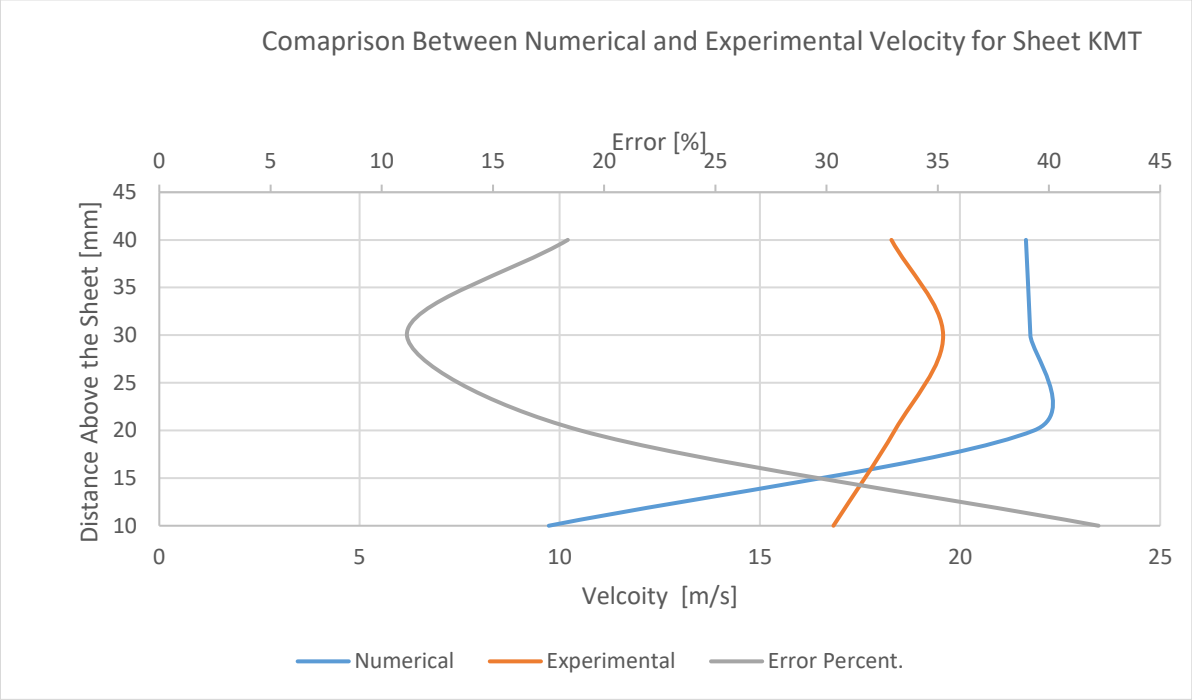


*Figure 64 Comparison between numerically and experimentally obtained Velocity for KMT sheet*

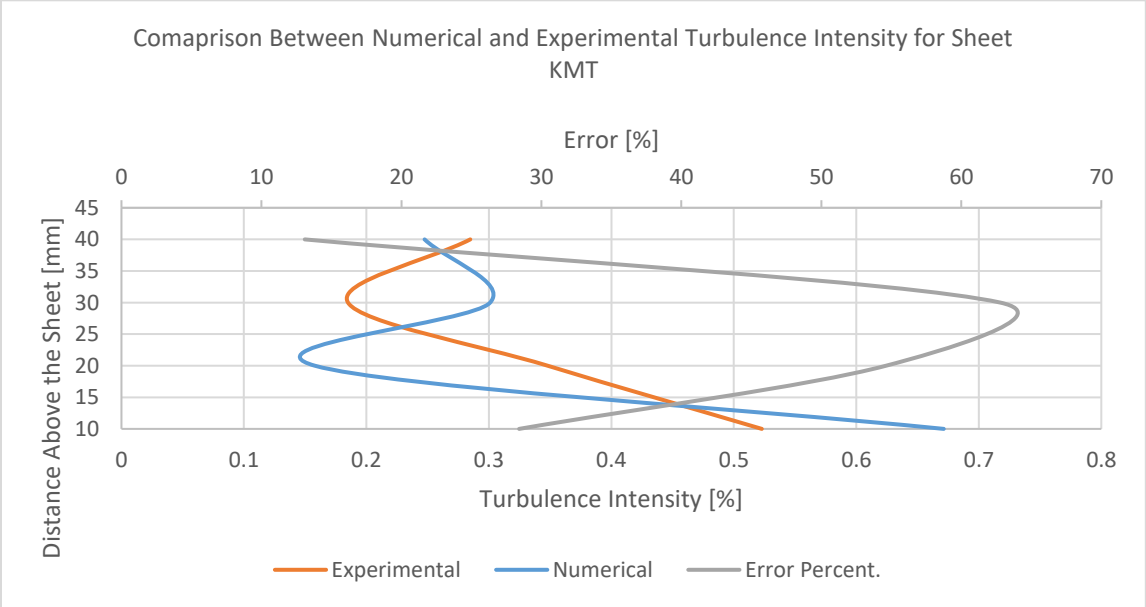


*Figure 65 Comparison between numerically and experimentally obtained Turbulence Intensity for KMT sheet*

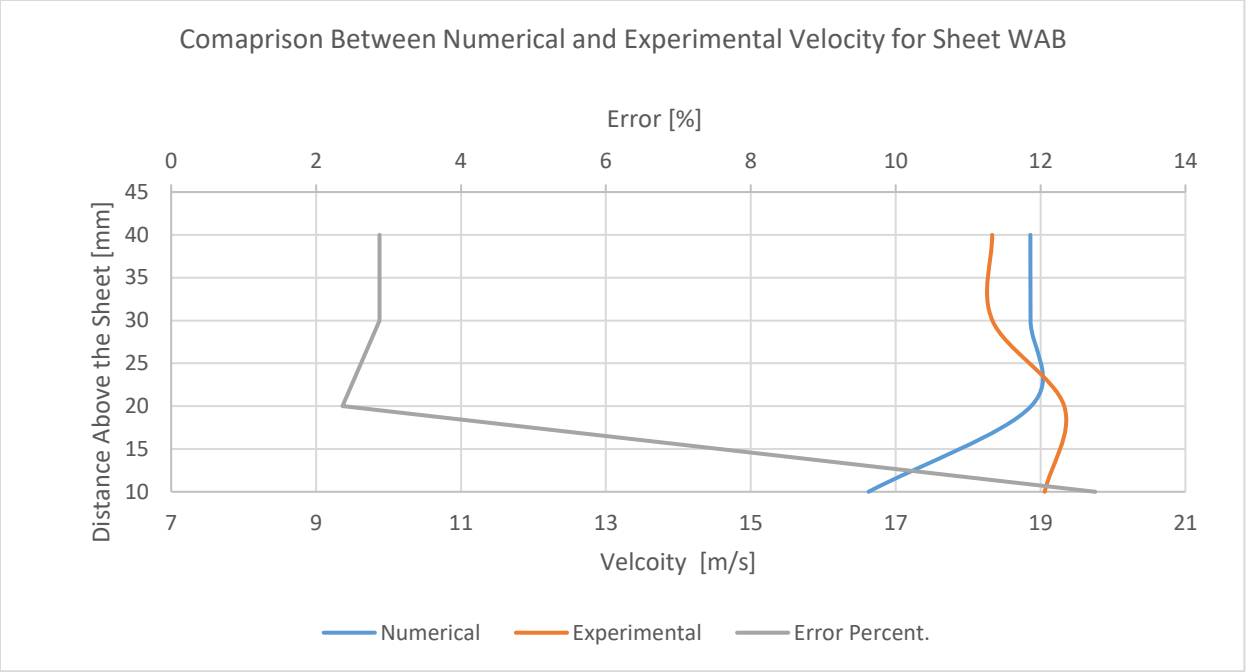


*Figure 66 Comparison between numerically and experimentally obtained Velocity for WAB sheet*

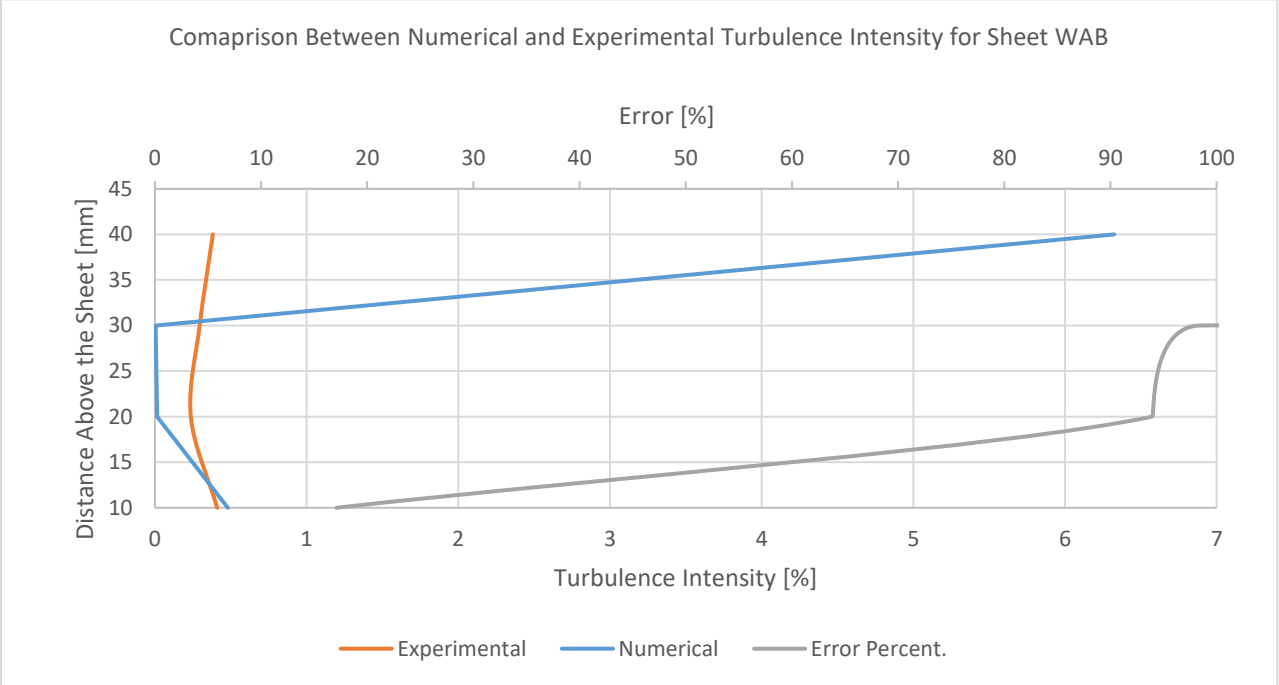


*Figure 67 Comparison between numerically and experimentally obtained Turbulence Intensity for WAB sheet*

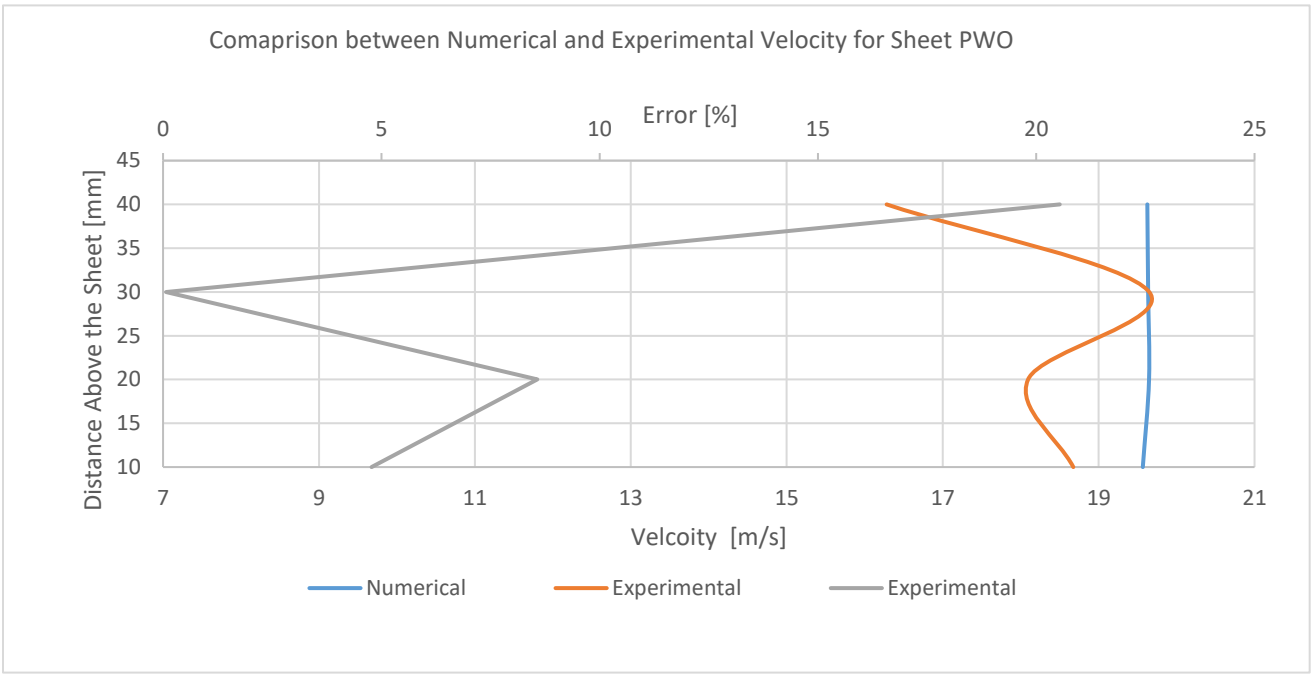


*Figure 68 Comparison between numerically and experimentally obtained Velocity for PWO sheet*

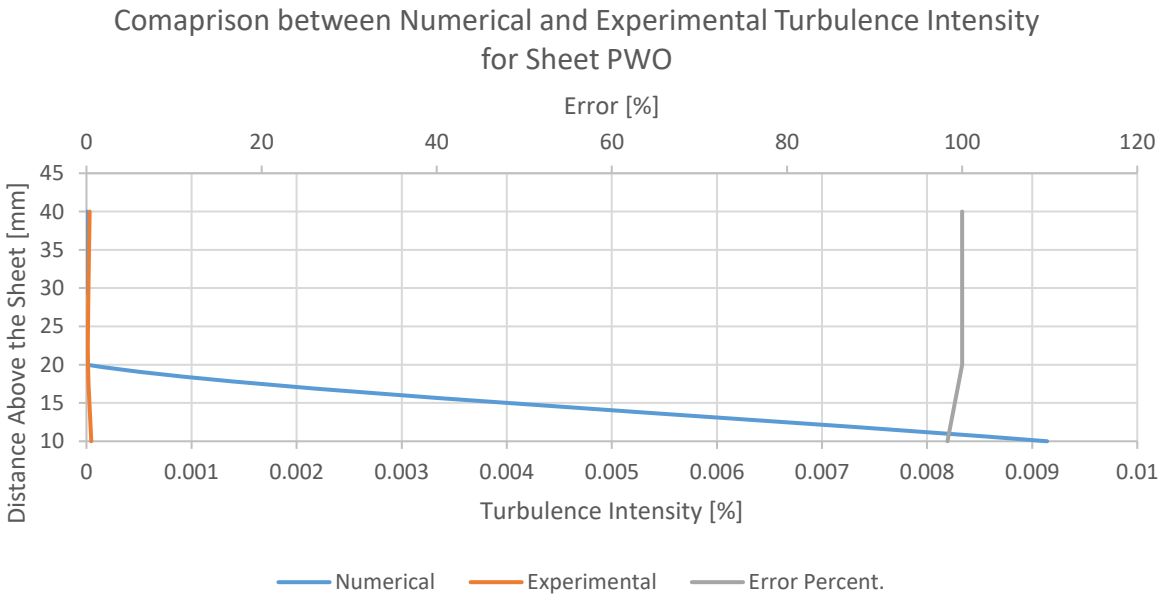


*Figure 69 Comparison between numerically and experimentally obtained Turbulence Intensity for PWO sheet*

# 5. Conclusion:

- Three sheets, KMT, WAB and PWO, of different structures have been investigated for the aero-acoustic performance. The investigation was done both experimentally and numerically.
- It was found experimentally by the microphone that the KMT sheet was of least sound.
- Sheet WAB has the smoothest velocity change across height. The velocity contours obtained from simulation reveals that WAB sheet also had the largest boundary layer.
- At maximum inlet flow velocity, Sheet PWO has the strongest velocity fluctuations over time followed by KMT followed by WAB according to the comparison of FFT of velocity after sheet trailing edge.
- The numerical simulation was performed using Ansys fluent using LES turbulence model. The analysis managed to capture the flow generated eddies causing the sound generation. The simulation of a single sheet usually needs computation time of around 48 hours to resolve the different frequencies obtained from the experiment.
- Using fluent tool of Fwocs & Hawkings model, it was possible to find agreements in the trend of the acoustic results between the numerical and experimental approaches over some frequency ranges. However, the two sets of results are shifted from each other. This may be due to inaccuracy in the acoustic tests. To avoid such inaccuracies, it is recommended to perform the tests in acoustically isolated rooms.
- There were big deviations between numerical and experimental results of turbulence intensity. This may be due to the difference in time steps of numerical simulation, 2.5e-5 sec. and of measurements, 0.07 seconds.
- Fluent is a powerful tool to simulate the aero-acoustic. However, its student version imposes restrictions over the mesh size. It would be advised to stick to an open source software like OpenFoam. It is worth mentioning that some work has started in the recent time to validate performance of OpenFoam in aero-acousitcs, an example can be found in [16].
- This work could have more area of development. For example, it would be interesting to perform the acoustic experiment and view eddies in the flow using Particle Image Velocimetry.

# *Bibioography:*


[1] MATIJEVIĆ, Dejan V. a Vladimir M. POPOVIĆ. Overview of modern contributions in vehicle noise and vibration refinement with special emphasis on diagnostics. *FME Transactions* [online]. 2017, **45**(3), 448–458. ISSN 14512092. Dostupné z: doi:10.5937/fmet1703448M

[2] GLOERFELT, Xavier. *Noise from automotive components* [online]. B.m., 2009. b.n. Dostupné z: http://sin-web.paris.ensam.fr/squelettes/ref_biblio/Gloerfelt_VKI_2009b.pdf

[3] WANG, Yiping, Zhengqi GU, Weiping LI a Xiaohui LIN. Evaluation of aerodynamic noise generation by a generic side mirror. *Proceedings of the World Academy of Science, …* [online]. 2010, **4**(1), 1288–1295. ISSN 2010376X. Dostupné z: http://citeseerx.ist.psu.edu/viewdoc/download?doi=10.1.1.193.112&rep=rep1&type=pdf

[4] YOKOYAMA, Hiroshi, Takahiro NAKAJIMA, Taishi SHINOHARA, Masashi MIYAZAWA a Akiyoshi IIDA. Aerodynamic noise produced in flow around an automobile bonnet. 2014, 1–8.

[5] *Occupational exposure to noise evaluation, prevention and control 13* [online]. Dostupné z: doi:10.1002/ejoc.201200111

[6] TINGAY, James. *What are A, C & Z Frequency Weightings?* [online]. Dostupné z: https://www.cirrusresearch.co.uk/blog/2011/08/what-are-a-c-z-frequency-weightings/

[7] *frequency-weightings-for-sound-level-measurements @ www.nti-audio.com* [online]. Dostupné z: http://www.nti-audio.com/en/support/faq/frequency-weightings-for-sound-level-measurements.aspx

[8] GOELZER, B., H. COLIN a A. GUSTAV. Noise Sources. *Federal Institute for Occupaational Safety and Health, Dortmund* [online]. 2001, 334. ISSN 0196-6553. Dostupné z: doi:10.1002/ejoc.201200111

[9] LIGHTHILL. *20. Aerodynamic Generation of Sound* [online]. 1952. Dostupné z: https://www.youtube.com/playlist?list=PL0EC6527BE871ABA3

[10] SHI, Lei, Zhibin YU a Artur J JAWORSKI. *Investigation into the Strouhal numbers associated with vortex shedding from parallel-plate thermoacoustic stacks in oscillatory flow.* 2011.

[11] LIU, Jiawei. *Simulation of Whistle Noise Using Computational Fluid Dynamics and Acoustic Finite Element*. 2012.

[12] *aerodynamic sound* [online]. 2002. Dostupné z: https://encyclopedia2.thefreedictionary.com/_/cite.aspx?url=https%3A%2F%2Fencyclopedia2.thefreedictionary.com%2Faerodynamic%2Bsound&word=aerodynamic sound&sources=MGH_cep,SciTech

[13] NEBENFUHR, Bastian. *OpenFOAM : A tool for predicting automotive relevant flow fields*. B.m., 2010. b.n.

[14] ANSYS, Inc. *ANSYS FLUENT 12.0 User's Guide* [online]. 2009. ISBN 0001-690X. Dostupné z: doi:10.1111/j.1600-0447.2011.01711.x

[15] LOCKARD, DP. *An overview of computational aeroacoustic modeling at NASA Langley* [online]. 1999. Dostupné z: http://scholar.google.com/scholar?hl=en&btnG=Search&q=intitle:An+overview+of+computational+aeroacoustic+modeling+at+nasa+langley+d#0

[16] SCHMALZ, J a W KOWALCZYK. Implementation of Acoustic Analogies in OpenFOAM for Computation of Sound Fields. *Open Jurnal of Acoustics* [online]. 2015, **5**(June), 29–44. ISSN 2162-5786. Dostupné z: doi:10.4236/oja.2015.52004

# Appendices:

## Appendix A:

**Code : A**

```
clc

clear all

close all

pkg load io



graphics_toolkit('gnuplot')

scrsz = get (0, "screensize");

plotvisible = 0 ; % yes - 1, no - 0


FFT('k','KMT','0','20',plotvisible,scrsz)

FFT('k','KMT','0','30',plotvisible,scrsz)

FFT('k','KMT','0','40',plotvisible,scrsz)

FFT('k','KMT','0','45',plotvisible,scrsz)


FFT('k','KMT','1','15',plotvisible,scrsz)

FFT('k','KMT','1','20',plotvisible,scrsz)

FFT('k','KMT','1','30',plotvisible,scrsz)

FFT('k','KMT','1','40',plotvisible,scrsz)

FFT('k','KMT','1','45',plotvisible,scrsz)


FFT('k','KMT','2','15',plotvisible,scrsz)

FFT('k','KMT','2','20',plotvisible,scrsz)

FFT('k','KMT','2','30',plotvisible,scrsz)

FFT('k','KMT','2','40',plotvisible,scrsz)

FFT('k','KMT','2','45',plotvisible,scrsz)


FFT('k','KMT','3','15',plotvisible,scrsz)

FFT('k','KMT','3','20',plotvisible,scrsz)
```

```
FFT('k','KMT','3','30',plotvisible,scrsz)
FFT('k','KMT','3','40',plotvisible,scrsz)
FFT('k','KMT','3','45',plotvisible,scrsz)

FFT('k','KMT','4','15',plotvisible,scrsz)
FFT('k','KMT','4','20',plotvisible,scrsz)
FFT('k','KMT','4','30',plotvisible,scrsz)
FFT('k','KMT','4','40',plotvisible,scrsz)
FFT('k','KMT','4','45',plotvisible,scrsz)

FFT('p','PWO','0','20',plotvisible,scrsz)
FFT('p','PWO','0','30',plotvisible,scrsz)
FFT('p','PWO','0','40',plotvisible,scrsz)
FFT('p','PWO','0','45',plotvisible,scrsz)

FFT('p','PWO','1','20',plotvisible,scrsz)
FFT('p','PWO','1','30',plotvisible,scrsz)
FFT('p','PWO','1','40',plotvisible,scrsz)
FFT('p','PWO','1','45',plotvisible,scrsz)

FFT('p','PWO','2','20',plotvisible,scrsz)
FFT('p','PWO','2','30',plotvisible,scrsz)
FFT('p','PWO','2','40',plotvisible,scrsz)
FFT('p','PWO','2','45',plotvisible,scrsz)

FFT('p','PWO','3','20',plotvisible,scrsz)
FFT('p','PWO','3','30',plotvisible,scrsz)
FFT('p','PWO','3','40',plotvisible,scrsz)
FFT('p','PWO','3','45',plotvisible,scrsz)

FFT('p','PWO','4','20',plotvisible,scrsz)
FFT('p','PWO','4','30',plotvisible,scrsz)
FFT('p','PWO','4','40',plotvisible,scrsz)
FFT('p','PWO','4','45',plotvisible,scrsz)

FFT('w','WAB','0','20',plotvisible,scrsz)
```

```
FFT('w','WAB','0','30',plotvisible,scrsz)
FFT('w','WAB','0','40',plotvisible,scrsz)
FFT('w','WAB','0','45',plotvisible,scrsz)

FFT('w','WAB','1','20',plotvisible,scrsz)
FFT('w','WAB','1','30',plotvisible,scrsz)
FFT('w','WAB','1','40',plotvisible,scrsz)
FFT('w','WAB','1','45',plotvisible,scrsz)
FFT('w','WAB','2','20',plotvisible,scrsz)
FFT('w','WAB','2','30',plotvisible,scrsz)
FFT('w','WAB','2','40',plotvisible,scrsz)
FFT('w','WAB','2','45',plotvisible,scrsz)

FFT('w','WAB','3','20',plotvisible,scrsz)
FFT('w','WAB','3','30',plotvisible,scrsz)
FFT('w','WAB','3','40',plotvisible,scrsz)
FFT('w','WAB','3','45',plotvisible,scrsz)

FFT('w','WAB','4','20',plotvisible,scrsz)
FFT('w','WAB','4','30',plotvisible,scrsz)
FFT('w','WAB','4','40',plotvisible,scrsz)
FFT('w','WAB','4','45',plotvisible,scrsz)
```

**Code : B**

```
function FFT(sh,sheet,n,hz,plotvisible,scrsz)
pkg load io
close all
rawdata=xlsread([sh n  hz '.xlsx'],'B2:C100000');
Lngth=length(rawdata(:,2));   %size of the time domain data
Ts=rawdata(Lngth,1)/Lngth;  %sampling time
Fs=1/Ts;
Lngth2=2^(nextpow2(Lngth)+0);
hanned=rawdata(:,2).*hanning(Lngth);
ft1=fft(hanned,Lngth2);
ft2=ft1(1:0.5*Lngth2);
g=0:Lngth2/2-1;
r(:,1)=Fs*g'(:,1)/Lngth2;
```

```
r(:,2)=abs(ft2);
if plotvisible==0
  figure(1,'Position',[0,scrsz(4),scrsz(3)*.95,scrsz(4)*.85], 'visible','off')
  else
  figure(1,'Position',[0,scrsz(4),scrsz(3)*.95,scrsz(4)*.85])
  endif
  hold on
plot(r(:,1),r(:,2))
title({'FFT of Air Velocity for ' sheet ' at  Height of', n ' cm at fan speed of ' hz 'Hz'})
  xlabel ('Frequency [Hz]',"fontsize",20)
  ylabel ('Power Spectral Density ',"fontsize",20)
xlim([0 0.5])
ylim([0 1000])
  saveas (gcf,[ sheet ' @' n '@' hz 'Hz_FFT.png'])
  movefile ([ sheet ' @' n '@' hz 'Hz_FFT.png'],'FFT');

   r_temp=fopen([ sheet ' @' n '@' hz 'Hz_FFT.ods'],'w');
   %fprintf(r_temp,'%12s %6s \r\n' , 'Freq. [Hz]','FFT');
   fprintf(r_temp,'%6g %6g \r\n' ,  r');
   fclose(r_temp);
   movefile([ sheet ' @' n '@' hz 'Hz_FFT.ods'], 'FFT');
hold off
endfunction
```

## Appendix B:

**Plots of Measured Velocity Signal in the Frequency Domain:**

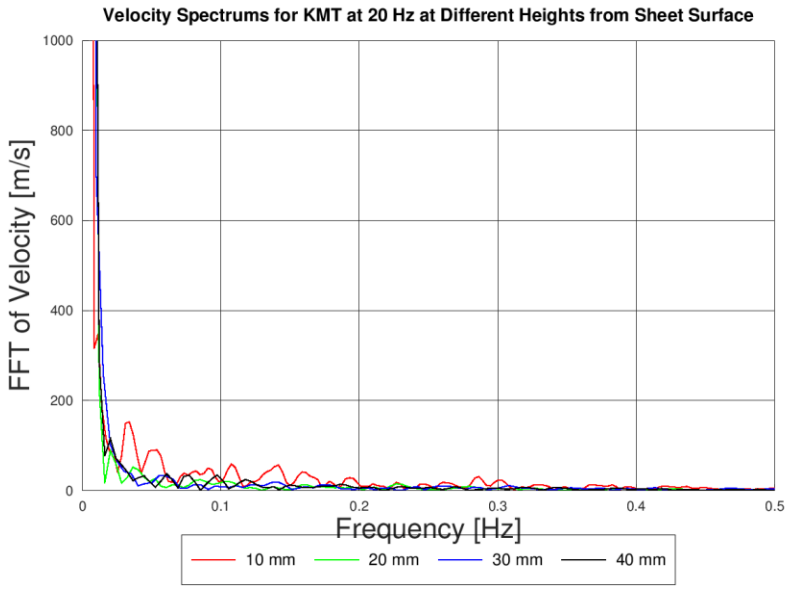


*Figure 70 Velocity Spectrum for KMT sheet at 20 Hz Ventilator Speed (inlet airspeed = 9.3 m/s)*

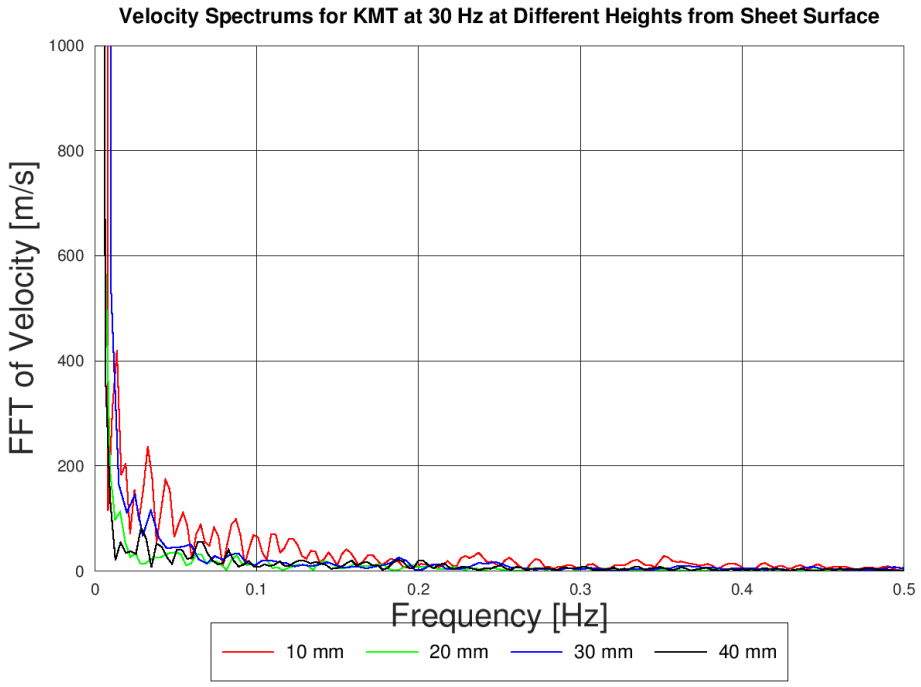


*Figure 71 Velocity Spectrum for KMT sheet at 30 Hz Ventilator Speed (inlet airspeed = 13.4 m/s)*

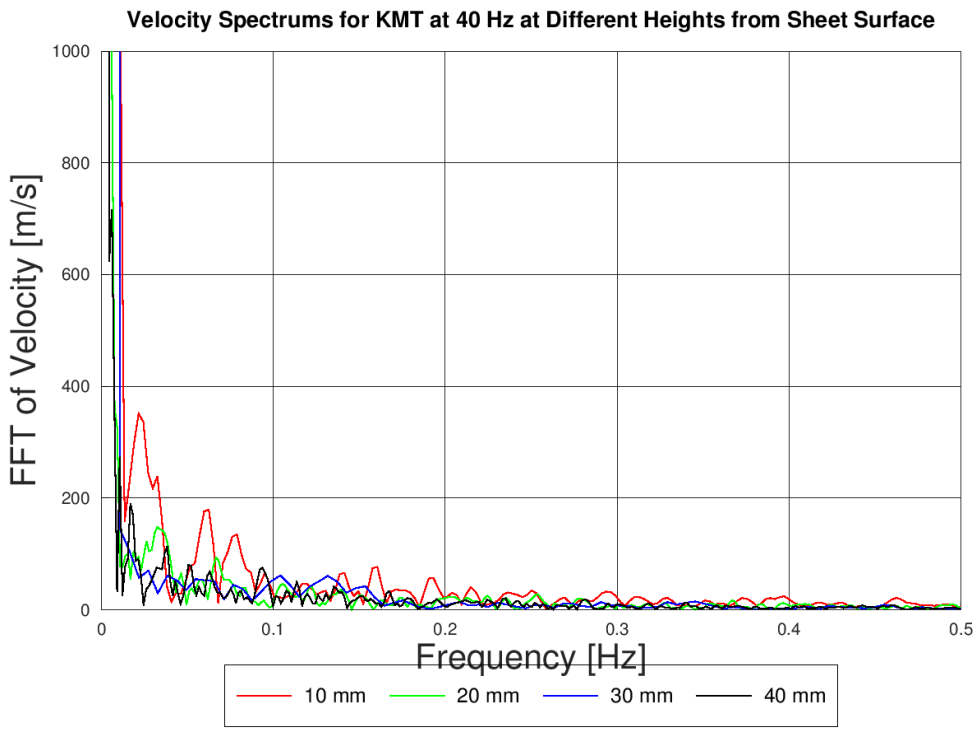


*Figure 72 Velocity Spectrum for KMT sheet at 40 Hz Ventilator Speed (inlet airspeed = 17.8 m/s)*

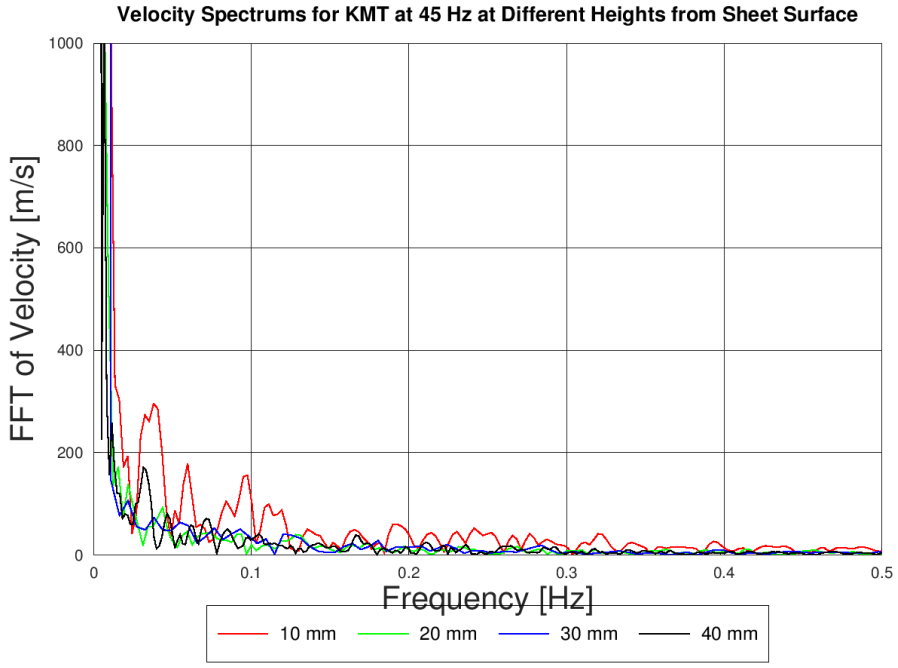


*Figure 73 Velocity Spectrum for KMT sheet at 45 Hz Ventilator Speed (inlet airspeed = 20.2 m/s)*

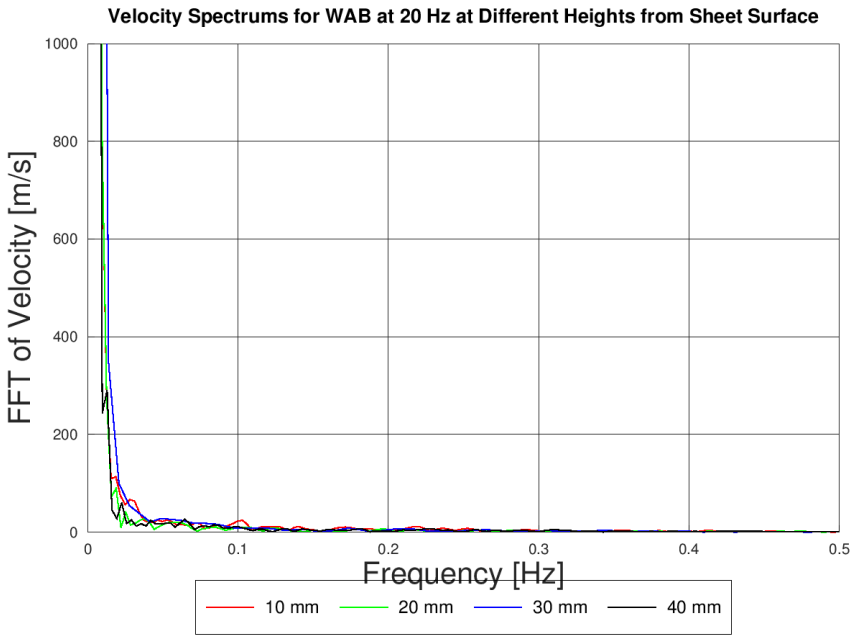


*Figure 74 Velocity Spectrum for WAB sheet at 20 Hz Ventilator Speed (inlet airspeed = 9 m/s)*

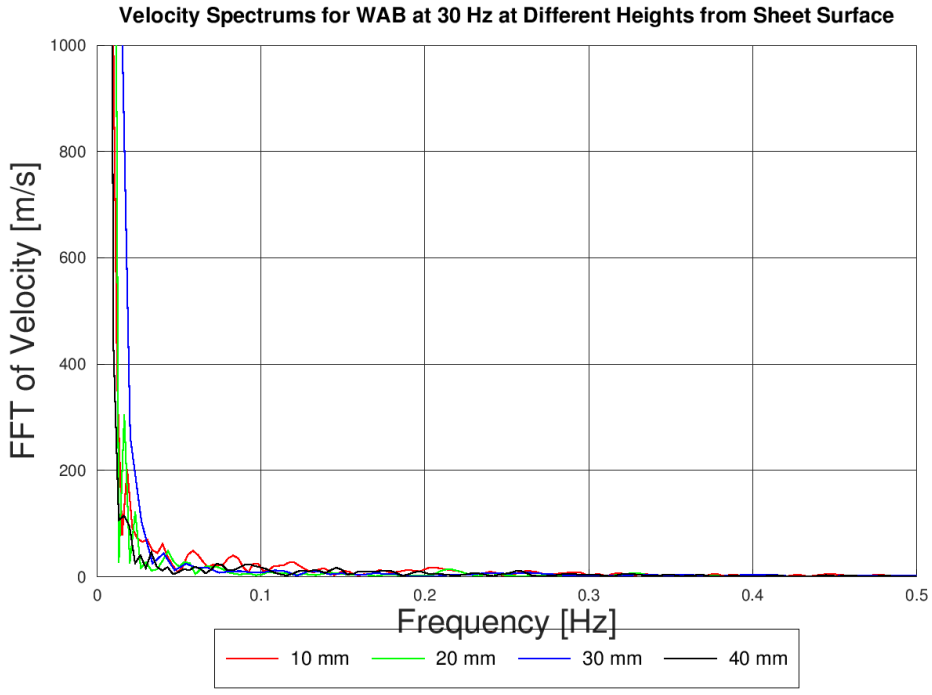


*Figure 75 Velocity Spectrum for WAB sheet at 30 Hz Ventilator Speed (inlet airspeed = 12.1 m/s)*

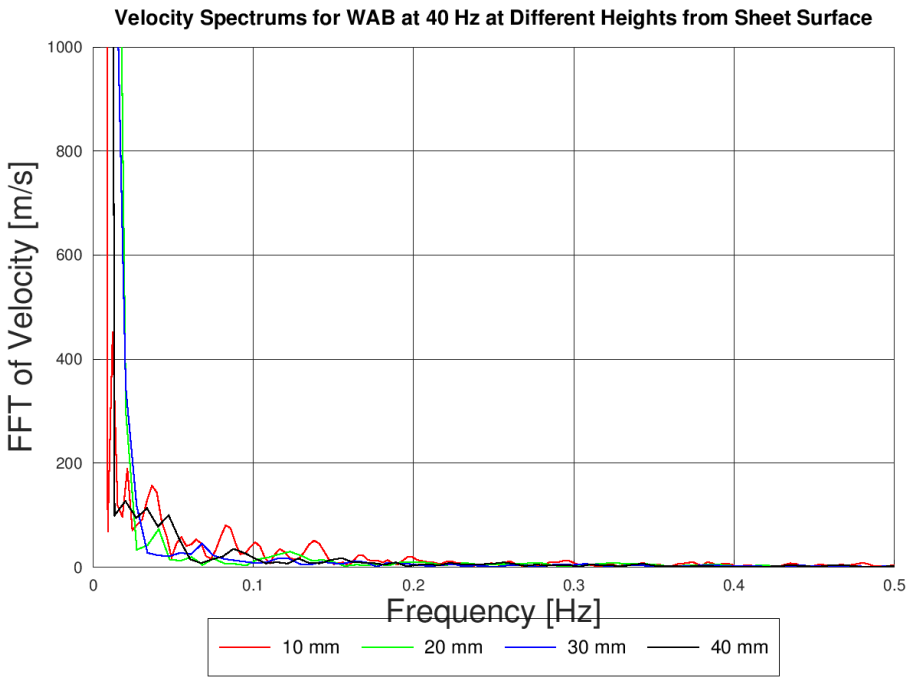


*Figure 76 Velocity Spectrum for WAB sheet at 40 Hz Ventilator Speed (inlet airspeed = 15.3 m/s)*

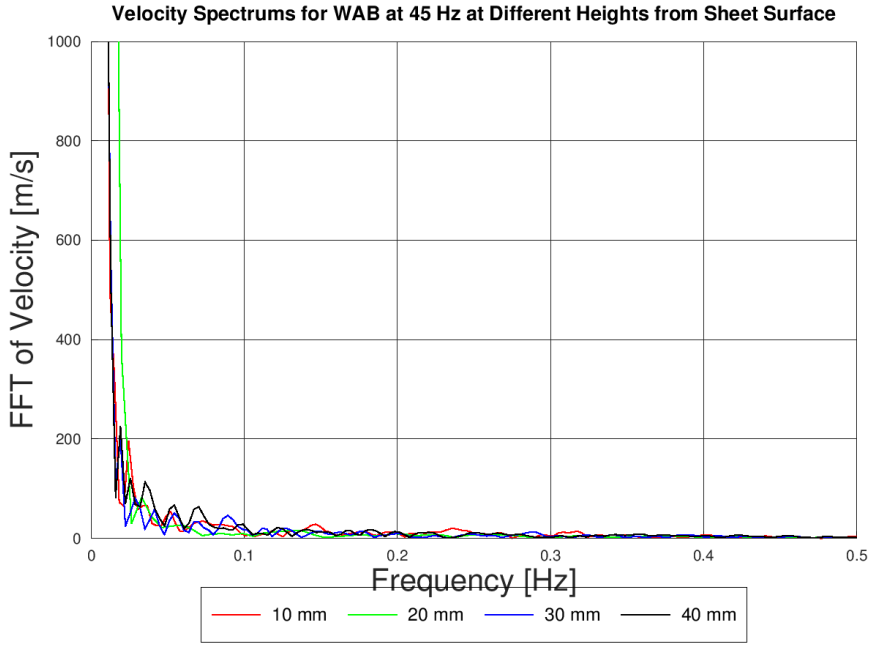


*Figure 77 Velocity Spectrum for WAB sheet at 45 Hz Ventilator Speed (inlet airspeed = 17 m/s)*

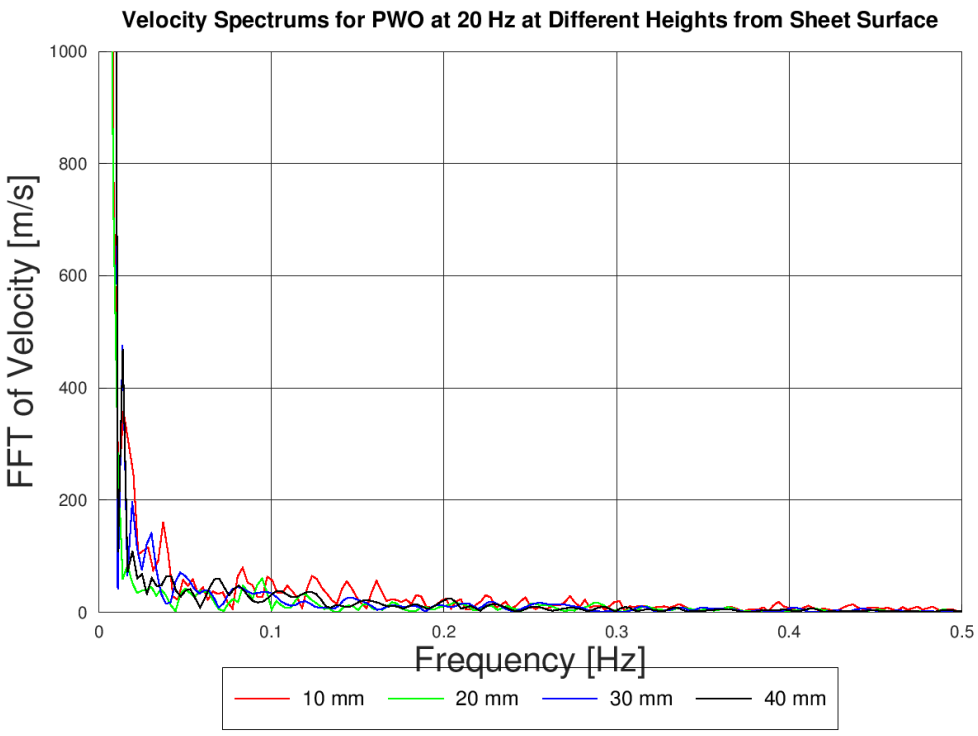


*Figure 78 Velocity Spectrum for PWO sheet at 20 Hz Ventilator Speed (inlet airspeed = 8.8 m/s)*

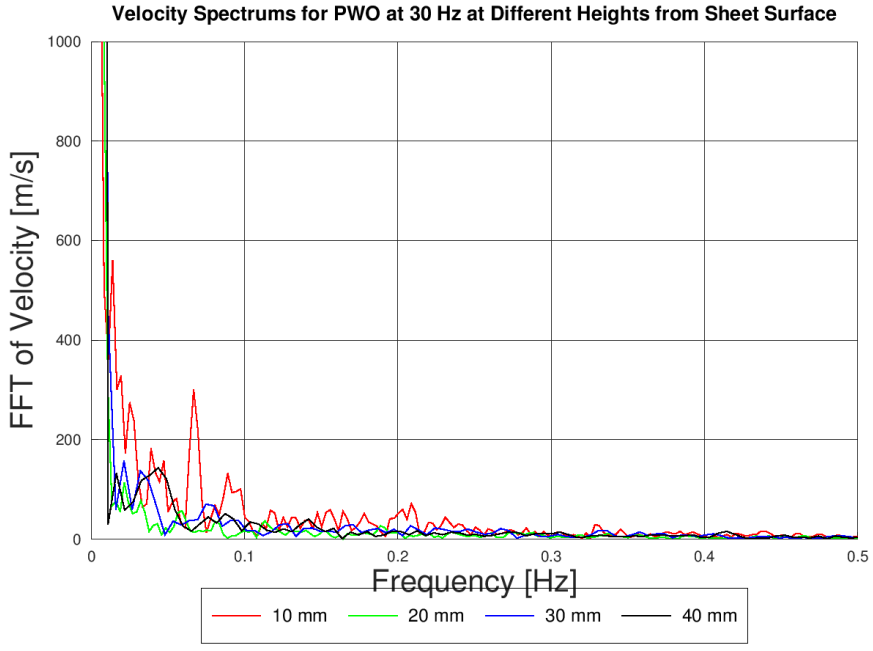


*Figure 79 Velocity Spectrum for PWO sheet at 30 Hz Ventilator Speed (inlet airspeed = 13.5 m/s)*

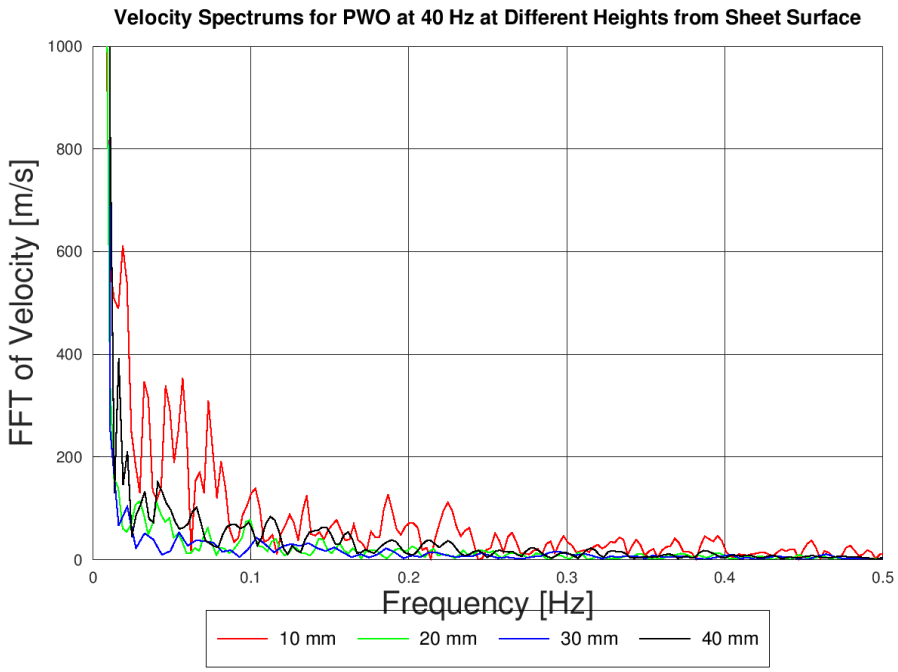


*Figure 80 Velocity Spectrum for PWO sheet at 30 Hz Ventilator Speed (inlet airspeed = 17.4 m/s)*

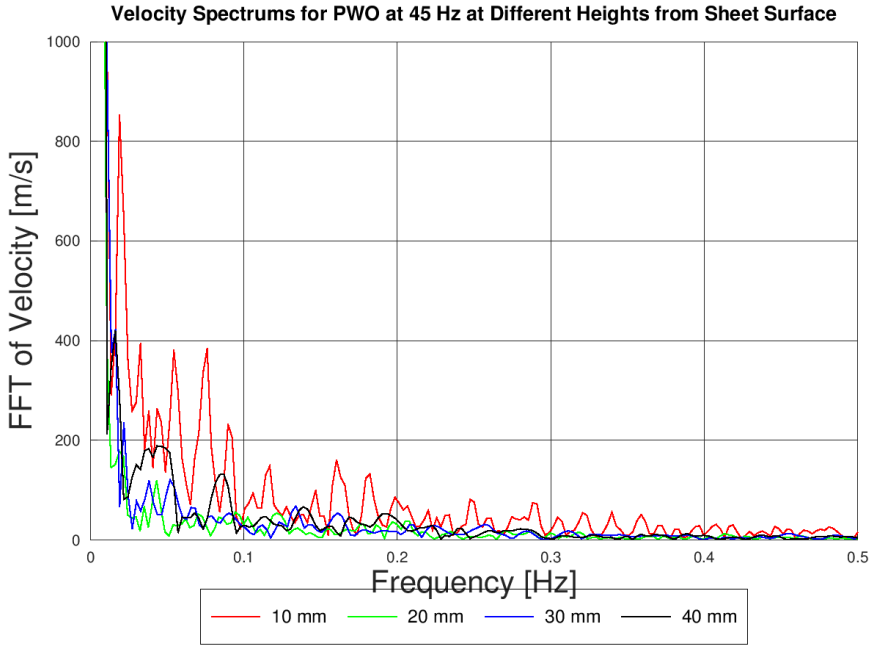


*Figure 81 Velocity Spectrum for PWO sheet at 30 Hz Ventilator Speed (inlet airspeed = 19 m/s)*